J. Earth Syst. Sci. (2017) 126:64
DOI 10.1007/s12040-017-0841-z

© Indian Academy of Sciences

Geochemistry and geochronology of the mafic dikes in the Taipusi area, northern margin of North China Craton: Implications for Silurian tectonic evolution of the Central Asian Orogen

Jing-Hua Wu[1], Huan Li[1,*], Xiao-Shuang Xi[2], Hua Kong[2], Qian-Hong Wu[2], Neng-Li Peng[3], Xi-Ming Wu[4], Jing-Ya Cao[2] and Jillian Aira S Gabo-Ratio[5]

[1]*Department of Resources Science and Engineering, China University of Geosciences, No. 388 Lumo Road, Wuhan 430 074, People's Republic of China.*
[2]*School of Geosciences and Info-Physics, Central South University, Changsha 410 083, People's Republic of China.*
[3]*Hunan Institute of Geological Survey, Changsha 410 016, People's Republic of China.*
[4]*Guangxi Land and Resources Planning Institute, Nanning 530 022, People's Republic of China.*
[5]*National Institute of Geological Sciences, University of the Philippines, Diliman, 1101 Quezon City, Philippines.*
**Corresponding author. e-mail: lihuan@cug.edu.cn*

MS received 18 October 2016; revised 10 February 2017; accepted 10 February 2017; published online 6 July 2017

The Taipusi area in the Bainaimiao Arc Belt is located in the northern margin of the North China Craton, at the southern margin of the middle Central Asian Orogenic Belt. It is characterized by large exposures of mafic dikes. In this contribution, we present first-hand whole-rock major and trace elements, zircon U–Pb geochronology and *in situ* trace element geochemistry data for these mafic rocks, which reveal their petrogenesis and tectonic evolution. These mafic dikes display varied compositions of SiO_2 (49.42–54.29%), TiO_2 (0.63–1.08%), Al_2O_3 (13.94–17.60%), MgO (4.66–10.51%), Fe_2O_3 (1.59–3.07%), FeO (4.60–6.90%), CaO (4.57–8.91%), Na_2O (1.61–4.26%), K_2O (0.92–2.54%) and P_2O_5 (0.11–0.29%). They are mainly of high-K calc-alkaline series with indistinct Eu anomalies, enriched in large ion lithophile elements (e.g., Rb, Ba, K and Sr) but depleted in high field strength elements (e.g., Nb, P and Ti). These suggest that the crystallizing magma was derived from enriched mantle altered by metasomatic fluids in a subduction setting with imprints of active continental margin features. The high concentrations of Hf, U, Th, Pb and Y, pronounced positive Ce but slightly negative Eu anomalies in zircons indicating that the magma underwent a fractional crystallization and crustal contamination process, with medium to high fO_2. Zircon LA–ICP–MS U–Pb dating yielded concordant ages of 437–442 Ma for these mafic dikes, which is consistent with the early Paleozoic volcanic arc magmatic activity in the Bainaimiao area. Hence, we conclude that the Bainaimiao Arc Belt is a continental arc formed by the southward subduction of the Paleo-Asian ocean during early Paleozoic.

Keywords. Mafic dikes; zircon U–Pb dating; tectonic setting; Bainaimiao Arc Belt; Central Asian Orogenic Belt.

1. Introduction

As one of the largest Phanerozoic orogenic accretionary belt in the world, the Central Asian Orogenic Belt (CAOB) is of great interest due to its long-term evolutionary history and complex tectonic magmatism (Windley *et al.* 2006). The Xing–Meng Orogenic Belt (XMOB), located at the eastern part of the CAOB within China, is about 2000 km long and 500 km wide and borders the Siberian Craton to the north and North China Craton to the south (figure 1a). Accompanied by widespread occurrence of various tectonic components, such as Precambrian microcontinents, Paleozoic island arcs, ophiolites, accretionary wedges, oceanic plateaus and successions of volcanic rocks, the XMOB has undergone multi-stage complex tectonic evolution, such as oceanic subduction, crustal accretion, multi-block collision and post-orogenic extension due to consumption of the Paleo-Asian Ocean (PAO) between the Paleozoic and the early Mesozoic (Sengör *et al.* 1993; Chen *et al.* 2000; Xiao *et al.* 2003). The XMOB tectonically consists of Northern Orogenic Belt (NOB), Solonker Suture and Southern Orogenic Belt (SOB) from the north to the south with several large linear faults as dividing lines (figure 1b; Khain *et al.* 2003; Jahn 2004; Xiao *et al.* 2004, 2009).

At the southern part of SOB, the E–W trending Bainaimiao Arc Belt (BAB) is located between Xilamulun fault and Chifeng–Baiyanobo fault (Jian *et al.* 2008). It is mainly composed of calc-alkaline tholeiitic basalts, felsic lavas, alkaline basalts, agglomerates, volcanic breccias, tuffs, granodiorites and granites (Zhao and Zhai 2013). The formation of the BAB is attributed mainly to the southward subduction of the PAO during the early Paleozoic, which led to the large-scale products of volcanic activity between Bainaimiao and Chifeng cities (Stampfli and Borel 2002). The formation, distribution and evolution of magmatism are closely related to the tectonic evolution of the area, and thus play a key role in identifying the tectonic environment. However, the space-time framework and tectonic setting of the early Paleozoic magmatism in the BAB have not yet reached unified understanding. The BAB has been identified as an island arc by many researchers (e.g., Jong *et al.* 2006) while others consider it as an Andean-type continental arc within the northern margin of North China Craton (e.g., Xiao *et al.* 2003); some researchers still suggest that there used to be a broad ocean that separated the northern NCC from BAB during the Cambrian–Ordovician period, which resulted in the formation of BAB (e.g., Zhang *et al.* 2014). In addition, previous studies in the area paid more attention to the geochemistry and geochronology of granite rocks in the western part of BAB. For example, U–Pb concordant ages of ~446 and ~443 Ma have been determined in Damaoqi and Bainaimiao, respectively (Zhang and Jian 2008; Feng *et al.* 2014). Due to the diverse granitic types and uncertain nature of magmatic source areas, the

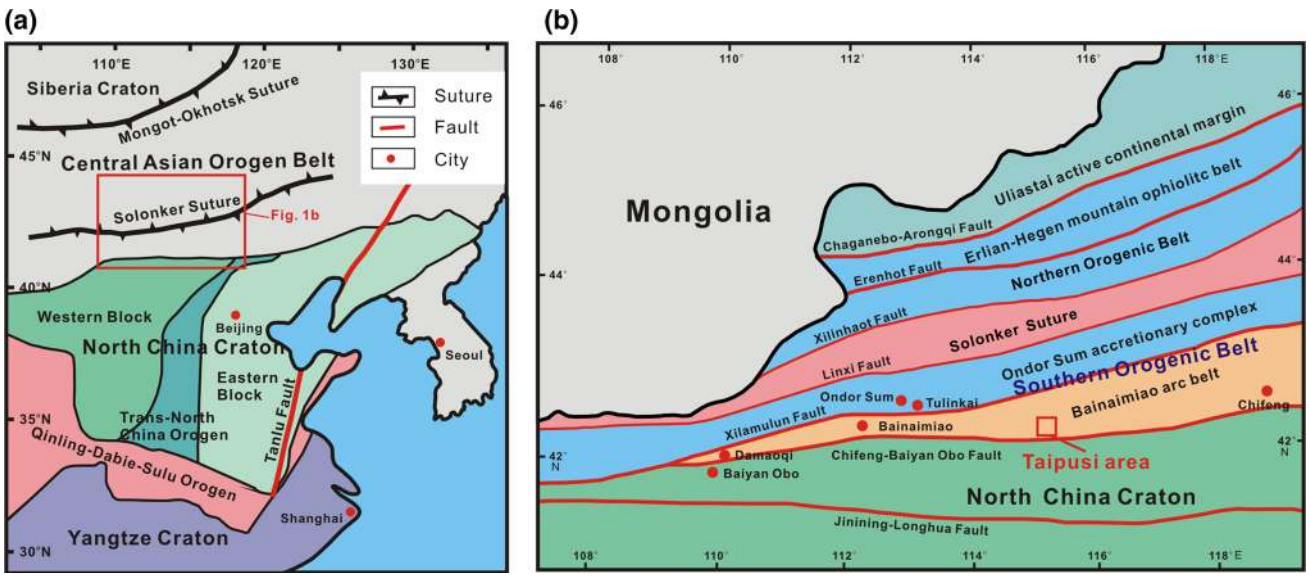

Figure 1. (**a**) Tectonic map of North China Craton and its adjacent areas (after Zhao *et al.* 2001) and (**b**) regional geological map of the Central Asian Orogenic Belt (after Xiao *et al.* 2003).

tectonic background of the Bainaimiao area is still controversial.

This study hopes to provide further constraints on this disputed tectonic environment from new approaches using local magmatic rocks. The Taipusi area is situated in the south of Xinlingol League, inner Mongolia autonomous region of North China, within the southmost middle segment of BAB. There have been limited geochemical and geochronological studies of mafic dikes in the middle part of Bainaimiao Arc Belt, which may host abundant information and provide constraints on the tectonic evolution of BAB.

Mafic rocks usually originate from the mantle and are closely related to mantle-derived rocks, which are associated with global tectonics (such as plate subduction and deep mantle processes). Thus, mafic rocks are of great significance in investigating source properties and analysing tectonic setting and deep kinetics of the lithosphere (Li *et al.* 2016). Furthermore, the study of the nature, source region, evolution, origin and dynamic background of mafic magma is the key to obtain information about related internal processes for further revealing magmatic generation and activity related to deep kinetic mechanisms. Based on field geological observation, the occurrence of the Taipusi area mafic dikes may be linked to the tectonic evolution of BAB.

Hence, based on comprehensive analysis of zircon U–Pb, geochronology and whole-rock, and zircon geochemistry, this study aims to reveal the origin and evolution of mafic magma in Taipusi area and provide new insights into the early Paleozoic tectonic evolution of BAB.

2. Regional tectonic evolution and geology

The northern margin of the NCC records a long history of crustal growth, tectonic evolution and stabilization from Archean to Paleoproterozoic (Santosh 2010; Zhao *et al.* 2010). During the Paleozoic, the northern margin of NCC was once strongly influenced by southward subduction of the Paleo-Asian ocean as indicated by surface tectonics and magmatism (Cope *et al.* 2005; Zhang *et al.* 2010). The consumption of PAO eventually led to the collision of North China Craton with the Siberia Craton, with Solonker Suture as the evidence for the termination of this collision–accretion process (Xiao *et al.* 2003). However, the tectonic model and time constraint for this subduction is still controversial. Based on detailed investigation of subduction- and collision-related magmas and forearc sediments in Solonker Suture zone, Chen *et al.* (2009) suggested that the opposing subduction of the PAO started from 530 Ma and ended between 296 and 234 Ma. In contrast, Jian *et al.* (2010) considered that the tectonic evolution for central southern CAOB can be classified into two independent subduction–collision processes that occurred during the early Paleozoic and also during the late Carboniferous–late Permian. Recently, a new model suggested that there used to be a southern subduction–collision system between North China Craton and Hunshandake Block during 500–440 Ma as well as a northern subduction–collision system between South Mongolia Microcontinent and Hunshandake Block during 500–380 Ma, resulting in the formation of SOB and NOB in 410 and 380 Ma, respectively (Xu *et al.* 2013). Until recent times, the closure of the Paleo-Asian ocean is postulated to have occurred between Permian and Triassic (Chen *et al.* 2000; Jian *et al.* 2008; Xiao *et al.* 2009). Although the existence of a Paleozoic subduction is an accepted fact, the formation, distribution and evolution of mafic rocks still require further investigation to provide more constraints in establishing the ancient tectonic environment of BAB.

The tectonic framework of XMOB and adjacent areas include several tectonic units from north to south, such as the Ulilastai Continental Margin, Erlian-Hegen Mountain Ophiolitic Belt, Northern Orogenic Belt (NOB), Solonker Suture and Southern Orogenic Belt (SOB) (figure 1b, Jian *et al.* 2008). The Erlian-Hegen Mountain ophiolitic complex is on the south of the Wuliang Yasi-Taiyuan continental margin, which consists of volcanic sedimentary strata, granite, blue schist, and a large number of ophiolites (Miao *et al.* 2008). The NOB is composed of Xilinhaot metamorphic complexes, Erdaojing complex, and two types of magmatic rocks associated with island arcs and collision features in Baolilao area (Xu *et al.* 2013). Representing the termination of the CAOB evolution in inner Mongolia, the Solonker Suture is marked by ophiolite exposures in the Sonlonker, Xiamulun and Linxi areas and separates XMOB into two orogenic belts (Jian *et al.* 2008). The area is bounded by Linxi fault to the north and Xilamulun fault to the south (Li *et al.* 2012a).

The main tectonic units of the SOB include the Bainaimiao Arc Belt (BAB) and the Ondor

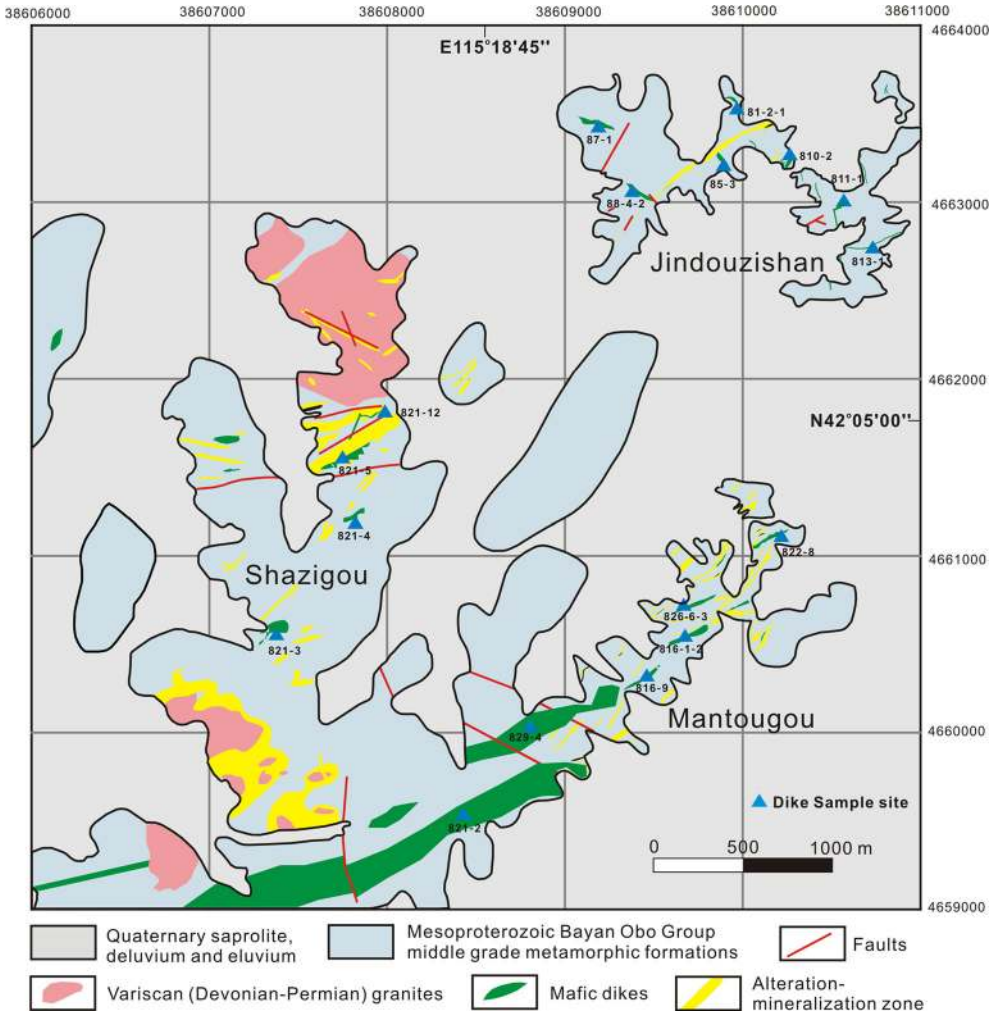

Figure 2. Simplified geological map of the Taipusi area (after Li *et al.* 2017).

Sum subduction–accretionary complex. The Ondor Sum complex is located to the north of the BAB and can be further subdivided into three units: underformed ophiolite belt, island arc complex, and mylonitized UHP subduction complex. The BAB is characterized by an assemblage of calc-alkaline tholeiitic basalts, felsic lavas, alkaline basalts, agglomerates, volcanic breccias, tuffs, granodiorites and granites (Xiao *et al.* 2003; Li *et al.* 2015). Four major geological units can be differentiated in the Bainaimiao area, namely a greenschist-facies volcano-sedimentary sequence, a low-P/T metamorphic complex, a mid-late Silurian flysch sequence and a late Silurian molasse (Zhang *et al.* 2013).

The exposed strata in the Taipusi area mainly belongs to the Mesoproterozoic Bayan Obo Group, with large exposures of Quaternary alluvium and limited exposures of Variscan granitic rocks (Devonian–Permian) (figure 2). The Bayan Obo Group structures trend NE–SW and consist of medium grade (partial to high grade) metamorphic formations. The photolytes are sedimentary clastic rocks, carbonate rocks and intermediate volcanic rocks. Divided into several lithologic sections, the Bayan Obo Group of the Taipusi area consists of garnet two-mica quartz schist, biotite quartz schist, marble, argillaceous slate, metamorphic feldspathic quartz sandstone, plagioclase amphibole schist, and banded migmatite. The Variscan granitic rocks are mainly medium-fine grained biotite-plagioclase granites and fine grained biotite adamellites, with intense silicification around the intrusive bodies. In addition, Permian–Triassic Mo polymetallic mineralization was formed in this area, with no obvious relationship with the outcropped magmatic rocks (Li *et al.* 2017).

The Taipusi area is characterized by widely distributed mafic dikes with different scales and occurrences (figure 2). They intruded into the Bayan

Obo Group along secondary fractures. These dikes mainly consist of gabbro, diabase and lamprophyre (figure 3a–b). The diabase and gabbro are mainly distributed in the southern and northeastern portions. The diabase is greyish-green in colour, has a massive structure and an ophitic texture with plagioclase (50%), pyroxene (30%) and hornblende (15%) as major minerals (figure 4a). The lamprophyre is dominantly located in the northern part of the ore field and has similar mineral composition exhibiting a porphyritic texture (figure 4b).

3. Sampling and analytical techniques

Different types of fresh mafic rocks were collected in the outcrops and exploratory trenches in the Taipusi area. Sampling locations of the representative samples are shown in figure 2.

Major elements were determined by X-ray fluorescence spectrometry. The FeO and Fe_2O_3 compositions were analysed using classical wet chemical method, followed by the measurement procedure described by Hey (1982). Standard samples were analysed to estimate precision, and the results indicated an error of <5%. Trace elements were analysed with an Agilent 7500a ICP-MS at the State Key Laboratory of Geological Processes and Mineral Resources, China, University of Geosciences, Wuhan, China. The detailed sample digestion procedure for the ICP-MS analysis, analytical precision and accuracy is similar to those described in Liu *et al.* (2008).

Diabase sample 821-12 and lamprophyre sample 826-1 were chosen for zircon U–Pb dating and trace element analysis. Zircon separation were carried out using standard techniques, purified by hand

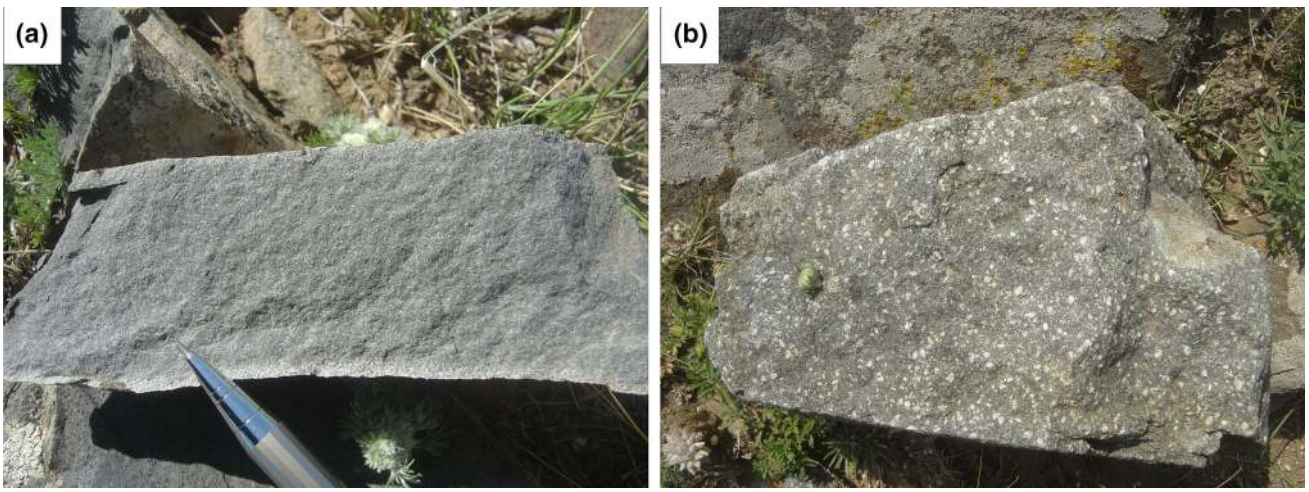

Figure 3. Field occurrences of diverse magmatic dikes in the Taipusi area (**a**) Diabase and (**b**) Gabbro.

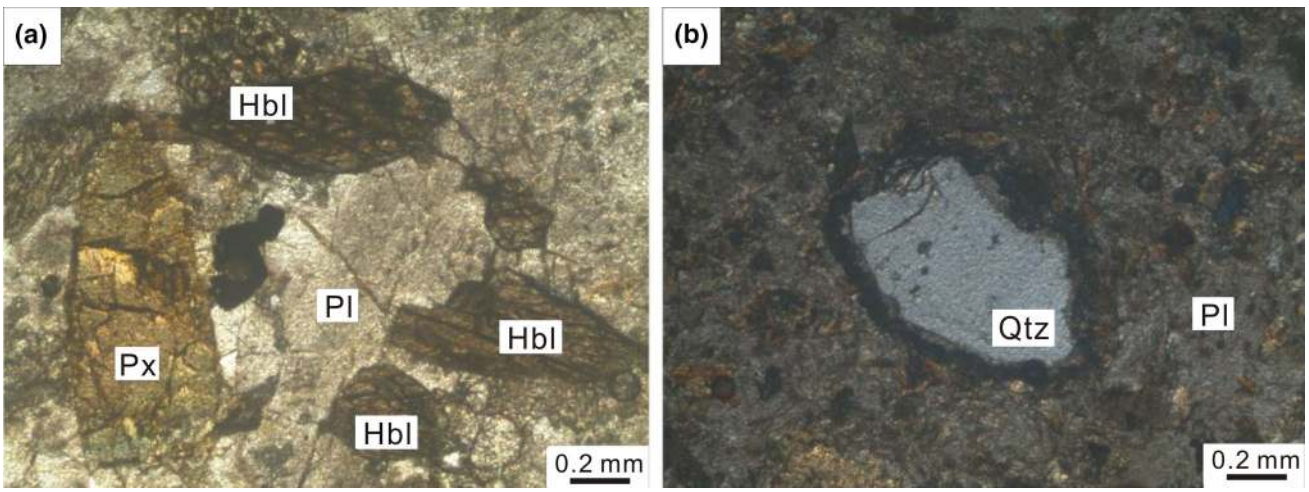

Figure 4. Micrograph images of the diverse magmatic dikes in the Taipusi area (**a**) Gabbro and (**b**) Lamprophyre. Px: pyroxene; Pl: plagioclase; Hbl: hornblende; Qtz: quartz.

picking under binocular microscope and mounted in epoxy resin and polished down to expose the grain center. Cathodoluminescence (CL) imaging was carried out at Northwest University (China), using a scanning electron microscope equipped with an energy dispersive spectroscopy system and a CL3+ detector under an operating condition at 15 kV and 20 nA. Typical CL images were obtained to identify internal structures and choose potential target sites for U–Pb and trace element analyses.

In-situ zircon trace element and U–Pb isotope analyses were performed at the State Key Laboratory of Continental Dynamics, Northwest University, China. An Agilent 7500a ICP–MS, equipped with a pulsed 193 nm ArF Excimer (Compex102) with laser power of 70 mj pulse energy at a repetition rate of 10 HZ, was used for ablation. The laser ablation beam diameter was 30 μm and the ablation depth was 20–40 μm. Helium was used as carrier gas to provide efficient aerosol transport to the ICP and minimize aerosol deposition. To correct laser induced fractionation, the SSB (Sample Standard Bracket) method was performed. Zircon 91,500 was used as an external standard to normalize isotopic fractionation during isotope analysis, and it was analysed twice for every 5 analyses. Meanwhile, NIST610 glass, which was analysed once every 10 analyses, was used as an external standard. Detailed descriptions of analytical procedure and instrumentation are given by Yuan *et al.* (2008). Off-line selection and integration of background and analytical signals, time-drift correction and quantitative calibration for U–Pb dating were performed using in-house software ICPMSDataCal (Liu *et al.* 2010), and the ^{204}Pb-based method was applied for common Pb correction (Andersen 2002). The ISOPLOT (version 4.15) program was employed for zircon concordant diagram plotting.

Zircon trace element concentration results were simultaneously obtained during zircon U–Pb dating. Combined with external standard NIST610, ^{91}Zr was used as an internal standard to correct trace element concentrations of the unknowns. A detailed calibration procedure for each element was presented in Liu *et al.* (2010). The preferred values of element concentrations for the standard sample NIST610 glass are from the GeoReM database (http://georem.mpch-mainz.gwdg.de/). The average analytical error ranges from ∼10% for light rare earth elements (LREE) to ∼5% for other trace elements.

4. Results

4.1 *Major and trace elements of rocks*

The major and trace element concentrations of 18 mafic rock samples from the Taipusi area are shown in table 1. The mafic rocks have varied chemical compositions in whole-rock geochemistry, with contents of SiO_2=49.42–54.29%, TiO_2=0.63–1.08%, Al_2O_3=13.94–17.60%, MgO=4.66–10.51%, Fe_2O_3=1.59–3.07%, FeO=4.60–6.90%, CaO=4.57–8.91%, Na_2O=1.61–4.26%, K_2O=0.92–2.54%, and P_2O_5=0.11–0.29%. Total alkali content (Na_2O + K_2O) was 2.53–6.01%, with an average value of 4.98%. A/CNK values range from 0.71–0.95, with an average value of 0.79. All of these imply a metaluminous signature for the mafic rocks. After the removal of LOI and recalculation of total major-element oxides into 100%, immobile elements (i.e., Ti, Zr, Y, Nb) are used to determine the rock types to eliminate the influence of the mobile alkaline elements. In the Zr/TiO_2–Nb/Y diagram, samples are plotted as andesite or basalt (figure 5a). Furthermore, the samples mostly plot in the calc-alkaline series field in the AFM diagram (figure 5b), and high-K calc-alkaline series and calc-alkaline series fields in the K_2O–SiO_2 diagram (figure 5c).

The total rare earth element (ΣREE) compositions of these mafic rocks range from 68.11 to 128.95 ppm, averaging at 91.95 ppm (table 1). The samples are characterized by the pronounced differentiation of LREE and HREE and the enrichment of LREE, with LREE/HREE and $(La/Yb)_N$ values ranging 4.97–8.96 and 4.58–9.88, respectively. REE patterns among different samples are similar to each other, with inclined lines for LREE but flat curves for HREE (figure 6a). The Eu and Ce negative anomalies are relatively weak, with average Eu/Eu* and Ce/Ce* values of 0.94 and 0.91, respectively.

On primitive mantle-normalized multi-element diagrams (figure 6b), these mafic rock samples show enrichment in large ion lithophile elements (LILE) (e.g., Rb, Ba, K and Sr) and depletion in high field strength elements (HFSE) (e.g., Nb, P and Ti).

4.2 *U–Pb geochronology*

The zircon CL images of sample 821-12 and 826-1 are present in figure 7. The typical oscillatory zoning of these zircons indicate that they are

Table 1. *Major and trace element compositions and related calculating parameters for the mafic dikes from the Taipusi area.*

Sample no.	816-9	821-1	826-6-3	821-5	821-3	829-4	821-12	821-2	822-8
SiO_2 (%)	53.18	53.82	50.18	51.28	50.05	54.21	50.85	52.60	54.29
TiO_2	0.75	0.96	0.87	0.98	1.07	0.78	1.00	0.74	0.78
Al_2O_3	14.6	16.9	14.5	16.0	16.0	15.6	15.4	15.5	14.7
Fe_2O_3	1.59	2.02	2.18	2.36	3.26	1.83	2.21	2.05	1.77
FeO	6.00	5.20	6.90	5.90	5.55	5.75	6.55	5.70	5.45
MnO	0.14	0.11	0.16	0.15	0.11	0.13	0.15	0.13	0.13
MgO	8.65	6.14	10.51	6.76	8.12	7.11	7.51	7.51	8.30
CaO	6.28	5.97	7.93	7.95	7.71	7.47	6.64	8.58	6.37
Na_2O	2.87	3.23	1.82	3.11	3.58	2.93	3.67	2.72	3.22
K_2O	2.28	2.54	2.17	2.14	1.66	1.25	2.30	1.46	2.00
P_2O_5	0.12	0.18	0.13	0.27	0.13	0.11	0.28	0.15	0.14
LOI	2.54	2.06	1.81	2.14	1.91	1.96	2.47	2.00	1.88
TOTAL	99.03	99.15	99.11	99.06	99.15	99.13	98.98	99.15	99.03
$Na_2O + K_2O$	5.15	5.77	3.99	5.25	5.24	4.18	5.97	4.18	5.22
A/NK	2.03	2.10	2.70	2.16	2.08	2.53	1.80	2.56	1.97
A/CNK	0.79	0.89	0.73	0.73	0.74	0.79	0.75	0.72	0.77
$Mg^{\#}$	67	61	68	60	63	63	61	64	68
FeO_{total}	7.43	7.02	8.86	8.02	8.48	7.40	8.54	7.54	7.04
La (ppm)	17.2	20.2	13.2	15.0	12.5	12.3	17.3	12.5	16.7
Ce	33.9	43.1	27.5	34.4	26.2	24.5	36.8	25.6	33.1
Pr	4.51	5.81	3.74	4.68	3.60	3.42	4.96	3.45	4.48
Nd	18.1	23.7	15.9	19.9	15.5	14.1	20.9	14.3	18.4
Sm	3.86	4.84	3.53	4.19	3.59	3.17	4.37	3.08	3.83
Eu	1.09	1.36	1.11	1.33	1.12	0.95	1.32	0.95	1.20
Gd	3.6	4.4	3.6	3.8	3.5	3.1	4.0	2.9	3.5
Tb	0.59	0.71	0.60	0.57	0.56	0.52	0.61	0.46	0.55
Dy	3.41	4.05	3.59	3.03	3.22	2.93	3.24	2.66	3.11
Ho	0.71	0.81	0.74	0.59	0.65	0.59	0.62	0.53	0.63
Er	1.89	2.20	2.01	1.53	1.68	1.54	1.61	1.43	1.66
Tm	0.29	0.34	0.31	0.23	0.26	0.24	0.25	0.22	0.26
Yb	1.90	2.15	1.95	1.43	1.58	1.51	1.57	1.37	1.59
Lu	0.32	0.35	0.32	0.23	0.25	0.25	0.26	0.23	0.26
ΣREE	91.34	114.00	78.02	90.87	74.18	69.07	97.76	69.69	89.23
LREE/HREE	6.18	6.60	4.97	6.97	5.34	5.49	7.07	6.09	6.69
Eu/Eu*	0.88	0.89	0.95	1.00	0.96	0.92	0.95	0.95	0.98
Ce/Ce*	0.89	0.92	0.91	0.96	0.90	0.88	0.92	0.90	0.89
La_N/Yb_N	6.12	6.35	4.58	7.09	5.35	5.51	7.47	6.15	7.06
Rb	111	153	332	82	64	61	86	66	88
Ba	801	787	173	960	346	309	636	386	466
Th	5.06	5.64	3.05	3.04	2.32	3.44	3.36	3.25	3.55
U	0.97	1.12	0.72	0.76	0.62	0.80	0.76	0.75	0.96
Ta	0.3	0.6	0.3	0.5	0.3	0.3	0.5	0.4	0.4
Nb	3.5	6.8	3.8	6.2	3.2	3.1	6.3	3.3	4.3
Sr	412	513	310	360	316	308	390	378	510
Zr	111	160	98	126	98	99	132	104	116
Hf	3.1	5.4	2.5	3.7	2.7	2.8	3.3	3.0	3.1
Y	18.9	20.7	18.2	15.1	16.0	15.3	15.9	12.9	16.4
Th/Ta	18.21	9.36	10.07	5.96	8.46	10.02	7.42	8.88	10.03
Nb/U	3.58	6.09	5.32	8.19	5.17	3.92	8.28	4.40	4.51
Nb/La	0.20	0.34	0.29	0.41	0.26	0.25	0.36	0.27	0.26
Nb/Ta	12.51	11.35	12.56	12.15	11.74	9.09	13.91	9.04	12.21
Zr/Hf	35.86	29.77	39.91	34.22	36.71	35.01	40.18	35.17	36.99
Nb/Yb	1.83	3.18	1.95	4.35	2.04	2.07	4.03	2.41	2.71
K*	4.76	3.82	5.41	4.15	4.42	3.16	4.21	3.58	4.04
Nb*	0.10	0.17	0.12	0.19	0.12	0.15	0.17	0.14	0.13
Sr*	1.20	1.16	1.08	1.00	1.14	1.20	1.02	1.44	1.50

Table 1. *(Continued.)*

Sample no.	81-2-1	85-3	87-1	88-4-2	810-2	813-1	816-1-2	821-4	811-1
SiO_2 (%)	54.02	50.85	53.36	50.91	50.03	53.39	52.86	50.56	49.42
TiO_2	0.75	1.06	0.63	0.95	1.08	0.78	0.77	0.81	1.07
Al_2O_3	15.0	17.0	15.4	16.3	17.6	16.1	17.0	13.9	16.2
Fe_2O_3	2.46	2.94	2.05	2.43	3.01	2.40	2.80	3.00	3.07
FeO	4.69	5.18	4.60	4.64	5.80	5.11	4.92	5.63	5.61
MnO	0.13	0.14	0.13	0.11	0.15	0.12	0.13	0.17	0.14
MgO	8.08	5.51	7.92	5.74	4.66	6.93	6.74	10.47	7.43
CaO	5.96	8.91	6.13	4.57	7.37	6.40	6.90	8.74	7.15
Na_2O	3.64	3.19	3.24	4.26	4.06	3.09	3.47	1.61	2.89
K_2O	1.81	1.82	1.69	1.75	1.89	1.53	1.42	0.92	2.41
P_2O_5	0.14	0.29	0.12	0.25	0.22	0.11	0.16	0.12	0.28
LOI	2.31	2.29	3.15	5.70	2.04	2.36	1.56	2.91	2.38
TOTAL	98.95	99.13	98.39	97.57	97.91	98.29	98.78	98.88	98.02
$Na_2O + K_2O$	5.45	5.01	4.93	6.01	5.95	4.62	4.89	2.53	5.30
A/NK	1.88	2.35	2.15	1.83	2.02	2.38	2.35	3.82	2.20
A/CNK	0.80	0.72	0.84	0.95	0.80	0.87	0.86	0.71	0.79
$Mg^{\#}$	68	56	69	60	49	63	62	69	61
FeO_{total}	6.91	7.83	6.44	6.82	8.51	7.27	7.44	8.33	8.37
La (ppm)	14.9	21.0	12.8	24.7	20.0	11.5	14.7	14.8	25.4
Ce	30.9	42.0	26.2	50.2	40.8	24.3	31.3	31.2	49.4
Pr	3.98	5.65	3.51	6.16	5.21	3.21	4.00	4.20	6.35
Nd	17.2	24.4	15.1	26.1	22.7	13.9	17.4	17.8	26.5
Sm	3.69	5.16	3.27	5.07	4.82	3.24	3.85	4.13	5.38
Eu	1.03	1.57	1.03	1.48	1.50	0.98	1.13	1.08	1.69
Gd	3.4	4.5	3.0	4.1	4.3	3.2	3.5	4.1	4.5
Tb	0.48	0.62	0.44	0.55	0.64	0.48	0.50	0.61	0.62
Dy	2.97	3.74	2.74	3.35	4.10	3.05	3.08	4.02	3.89
Ho	0.58	0.70	0.54	0.63	0.79	0.59	0.64	0.79	0.73
Er	1.69	1.90	1.58	1.84	2.43	1.71	1.81	2.35	2.06
Tm	0.23	0.26	0.21	0.26	0.33	0.23	0.26	0.32	0.29
Yb	1.57	1.71	1.39	1.69	2.22	1.54	1.73	2.18	1.90
Lu	0.24	0.26	0.21	0.24	0.33	0.22	0.24	0.32	0.28
ΣREE	82.84	113.50	72.05	126.40	110.19	68.11	84.12	87.85	128.95
LREE/HREE	6.44	7.27	6.11	8.96	6.27	5.20	6.17	5.00	8.06
Eu/Eu*	0.88	0.97	0.98	0.96	0.99	0.93	0.93	0.80	1.03
Ce/Ce*	0.93	0.89	0.91	0.93	0.92	0.93	0.94	0.92	0.89
La_N/Yb_N	6.41	8.30	6.22	9.88	6.09	5.05	5.74	4.59	9.03
Rb	72	59	74	69	53	65	46	71	97
Ba	460	478	382	1210	752	423	616	301	932
Th	3.92	3.54	3.04	4.89	4.52	3.12	3.04	3.92	4.57
U	0.88	0.81	0.82	1.03	0.93	0.70	0.64	0.75	0.96
Ta	1.2	0.9	1.9	0.6	1.6	0.6	2.6	1.3	2.8
Nb	5.1	7.3	4.2	5.8	6.3	3.2	3.9	5.2	8.5
Sr	588	416	716	782	707	388	569	358	500
Zr	114	130	100	132	112	96	112	97	148
Hf	3.2	3.4	2.9	3.6	3.2	2.8	3.2	2.9	3.9
Y	17.0	20.8	15.4	18.4	24.0	17.2	18.4	23.1	21.1
Th/Ta	3.27	3.93	1.60	8.15	2.83	5.20	1.17	3.02	1.63
Nb/U	3.58	6.09	5.32	8.19	5.17	3.92	8.28	4.51	5.80

Table 1. *(Continued.)*

Sample no.	81-2-1	85-3	87-1	88-4-2	810-2	813-1	816-1-2	821-4	811-1
Nb/La	0.34	0.35	0.33	0.23	0.32	0.28	0.27	0.35	0.33
Nb/Ta	4.25	8.11	2.21	9.67	3.94	5.33	1.50	4.00	3.04
Zr/Hf	35.63	38.24	34.48	36.67	35.00	34.29	35.00	33.45	37.95
Nb/Yb	3.25	4.27	3.02	3.43	2.84	2.08	2.25	2.39	4.47
K*	2.97	3.21	2.22	2.81	1.62	2.65	1.80	2.49	1.14
Nb*	0.15	0.18	0.13	0.15	0.21	0.15	0.11	0.17	0.25
Sr*	1.85	0.95	2.62	1.56	1.69	1.54	1.77	1.10	1.00

$Mg^{\#} = 100Mg^{2+}/(Mg^{2+} + FeO_{total})$, $FeO_{total} = FeO + 0.8998 \times Fe_2O_3$, $K^* = 2K_N/(Ta_N + La_N)$, $Nb^* = 2Nb_N/(K_N + La_N)$, $Sr^* = 2Sr_N/(Ce_N + Nd_N)$.

magmatic zircons. Most of the zircons are transparent but dark to slightly bright except 2 grains containing bright cores (No. 06 and 08 of sample 826-1). Grain size mainly varies from 70–120 μm, with aspect ratios 2:1 to 3:1 and euhedral to slightly rounded shapes, indicating that some of them are inherited zircons trapped by ascending magma.

The 33 spots of U–Pb analytical results from samples 821-12 and 826-1 are presented in table 2. There are large variations for the total Pb, ^{232}Th, ^{238}U contents and distinct $^{206}Pb/^{238}U$ ages ranging 435–2132 Ma. However, most of the ages cluster at ∼440 Ma while the other ages are scattered (figure 8a–d). Previous research suggested that a series of magmatic activities occurred in the NCC from the late Paleoproterozoic to Neoproterozoic: formation of a large igneous province (∼1.78 Ga), anorogenic magmatic activity (1.72–1.62 Ga), diabase sill intrusions (1.35–1.32 Ga) and mafic dyke swarm intrusions (∼900 Ma) (Zhai *et al.* 2014). Conforming to these magmatic events, the age of inherited zircons in the study reflect the assimilation of the old basement of NCC during magma ascent. After removing unreliable data with concordance less than 90%, the zircons dated ∼400–500 Ma can be considered representative of the formation age of the mafic rocks; while those with scattered and old ages may be inherited zircons. Eventually, 9 spots of 821-12 and 13 spots of 826-1 (noted as magmatic zircons in table 2) were selected to calculate the formation age of the diabase. Zircons from 821-12 yielded a concordant U–Pb age of 437.6±5.8 Ma (MSWD=0.25) and a weighted mean U–Pb age of 437.6±2.7 Ma (MSWD=0.33). Within the age error of sample 821-12, zircons from 826-1 gave a concordant age of 442.6±9.2 Ma (MSWD=0.18) and a weighted mean age of 440.5±2.3 Ma (MSWD=0.28) (figure 8e, f). Thus, the mafic rocks in the Taipusi area are estimated to have intruded during ∼440 Ma.

4.3 *Trace elements of zircons*

Magmatic zircon trace element analysis results are shown in table 3. Due to the similarity of the samples in element concentration, their geochemical characteristics are described together. These zircons have high average Hf values of 31,300 ppm. Titanium concentrations mainly vary from 10–33 ppm (averaging at 17 ppm) except one zircon possessing 465 ppm. In addition, these zircons have low average values of Nb (9.1 ppm) and Ta (4.1 ppm) concentrations. Meanwhile, the Th/U ratios are greater than 0.4 with an average value of 0.71.

The chondrite-normalized REE patterns of the zircons are strongly enriched in heavy REEs relative to light REEs (figure 9a, b). ΣREE concentrations range from 960 to 3853 ppm with an average value of 1956 ppm. These zircons possess medium negative Eu anomalies with Eu/Eu* varying from 0.16–0.68 (averaging 0.41) and pronounced positive Ce anomalies with Ce/Ce* ranging from 3.3–47.9 (averaging 25.7).

5. Discussion

5.1 *Timing of dikes in Taipusi area*

Dikes exposed in the Taipusi area are mainly composed of mafic rocks such as gabbro, diabase and lamprophyre. The zircons from these mafic rocks have long columnar, idiomorphic crystal shapes with high Th/U ratios. They show clear oscillatory zoning in CL images, indicating a magmatic origin. Hoskin (2005) demonstrated that there exists a distinct discrepancy of REE distribution patterns between magmatic zircons and hydrothermal zircons. Compared to magmatic zircons, hydrothermal zircons have flat LREE concentration patterns, higher REE concentration and slight positive Ce

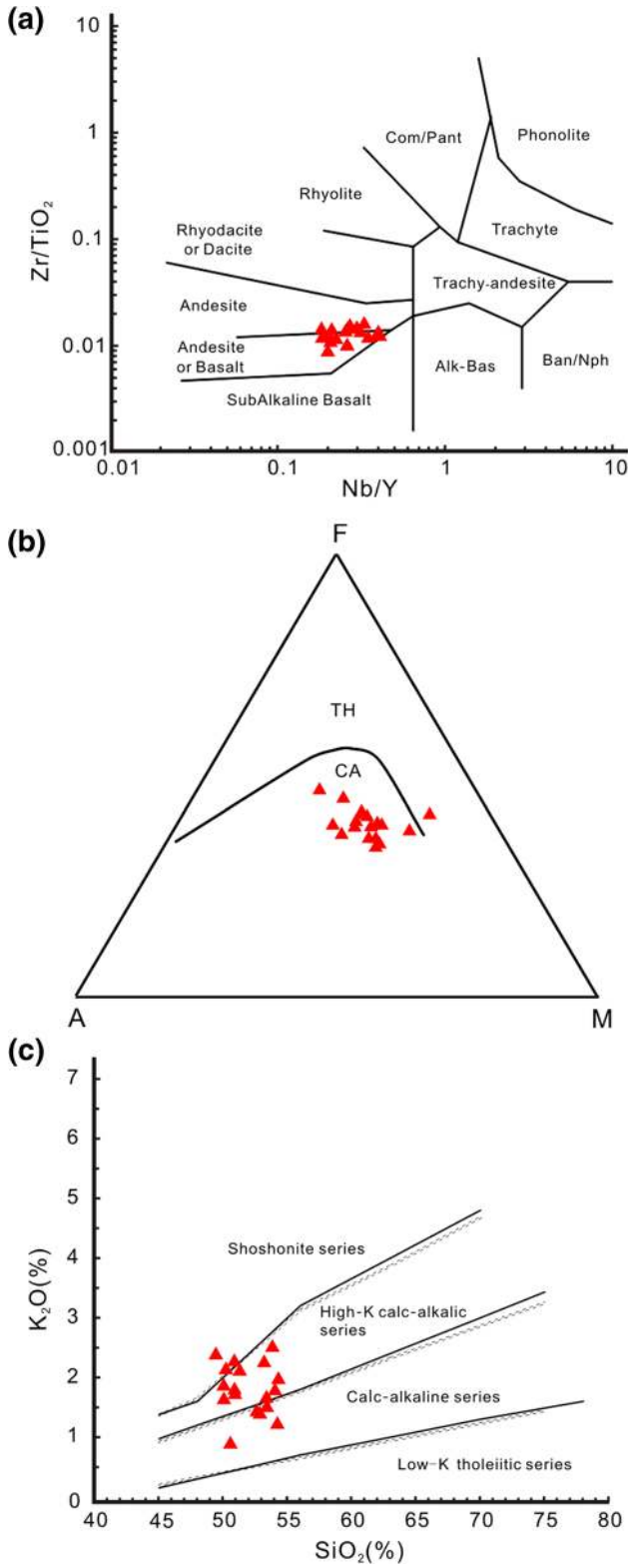

Figure 5. (**a**) Zr/TiO_2 *vs.* Nb/Y diagram (after Winchester and Floyd 1977), (**b**) AFM diagram (after Irvine and Baragar 1971), TH: tholeiite series; CA: calc-alkaline series and (**c**) SiO_2 *vs.* K_2O diagram (after Peccerillo and Taylor 1976).

anomaly. As shown in figure 9(a, b), all the zircons show typical features of magmatic zircons although several zircons with older ages display

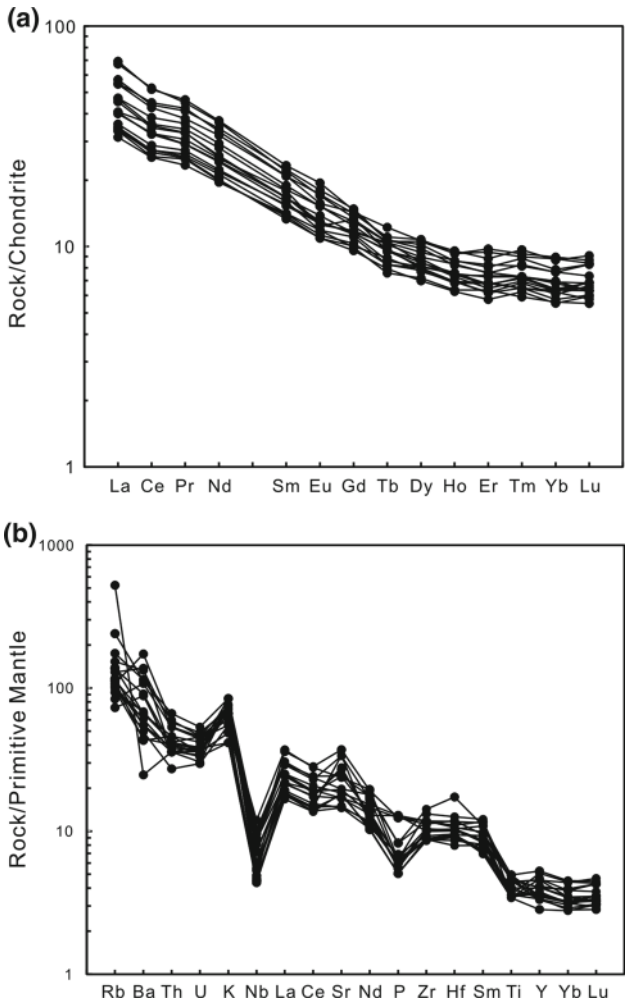

Figure 6. (**a**) Chondrite-normalized REE patterns for the mafic rocks from the Taipusi area. (**b**) Primitive mantle normalized trace element patterns for the mafic rocks from the Taipusi area. Normalized values for chondrite and primitive mantle are from Sun and McDonough (1989).

diverse patterns, implying they may be inherited zircons due to crustal contamination. The dating results show that the concordant ages of the diabase and lamprophyre are ~437 and ~442 Ma, respectively, which are within the error range. Numerous contemporaneous magmatic activities have been identified in the BAB area such as granodiorite porphyry (445±6 Ma) in Bainaimiao deposit, tonalite (446±3 Ma) and quartz diorite (438±4 Ma) in Siping–Yitong of NE China, and hornblende gabbro in Damaoqi area (Li *et al.* 2010, 2012b; Zhang *et al.* 2014). These isotopic data conform to U–Pb ages in this study, indicating that magmatism in BAB area have regional characteristics rather than influenced by local development. It confirms that the dating results are of high reliance, and thus formation period of these dikes is considered to be during the early Silurian.

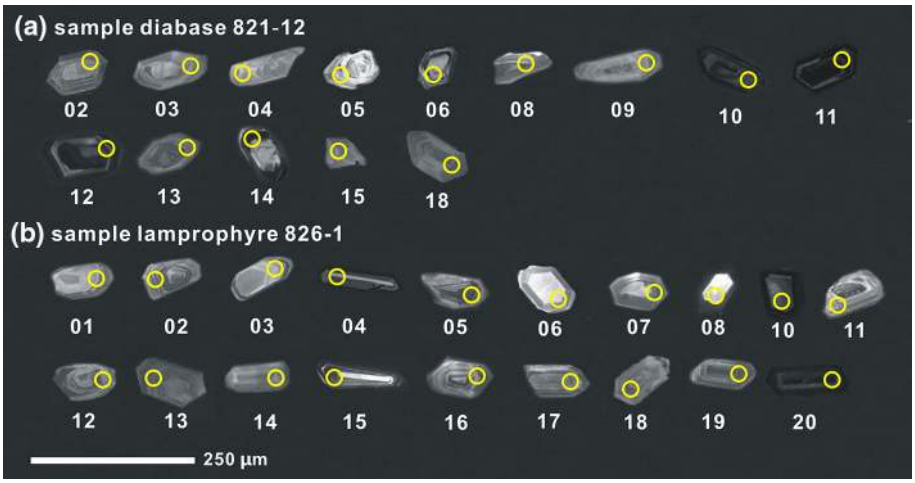

Figure 7. Zircon CL images of diabase sample 821-12 (**a**) and lamprophyre sample 826-1 (**b**) from the Taipusi area.

5.2 *Origin and evolution of the mafic magma*

5.2.1 *Whole-rock geochemical implications*

Most original mafic magmas formed by partial melting of the mantle do not undergo pronounced fractional crystallization and crustal contamination. Mafic rocks formed by original magmas are generally characterized by low compositions of SiO_2 and incompatible elements (e.g., LILE, HFSE and LREE), with Mg# values ranging from 65 to 75 (Jesus *et al.* 2014). Mafic rocks in Taipusi area are enriched in LILE and LREE but depleted in HFSE, with varied Mg# values ranging 49–69 (table 1), indicating the source region evolution may have an affinity with subduction zone magmatism.

The relationship between different major-element oxides is shown in figure 10. The negative correlation between MgO and Al_2O_3 indicates fractional crystallization of olivine during the magma evolutionary process (figure 10a), and the positive correlation of MgO *vs.* CaO and CaO *vs.* CaO/Al_2O_3 implies fractional crystallization of clinopyroxene (figure 10b, c). Additionally, the negative correlation of MgO *vs.* P_2O_5 and MgO *vs.* TiO_2 illustrates fractional crystallization of apatite and Ti–Fe oxides (figure 10d, e). The negative correlation between MgO and total alkaline (Na_2O+K_2O) also indicates fractional crystallization of other major and accessory minerals (figure 10f). In contrast, the slightly negative Eu anomalies (average $\delta Eu=0.94$) imply weak fractional crystallization of plagioclase.

Crustal contamination is an important evolutionary process during magma ascent. The enrichment of LILE and LREE, and the depletion of HFSE indicate that crustal materials were involved in the formation process of the mafic rocks in the Taipusi area, either at the source or during magma ascent and evolution (Wang *et al.* 2012; Zhao *et al.* 2014). The weak negative Ce anomalies (average $\delta Ce=0.91$) may imply that crustal materials with depleted Ce were incorporated into the magma. The depletion of Nb and Ta may indicate that crustal or source contamination occurred during the magma intrusive process. The Th/Ta ratios range from 1.17 to 18.21 (average 6.62) and are mostly higher than 2.07 value of primitive mantle (Sun and McDonough 1989), also suggesting pronounced crustal contamination. High primitive mantle-normalized Tb/Ta ratios ($(Tb/Ta)_N > 1$) and low Nb/La ratios ($Nb/La < 1$) are two reliable indicators for crustal contamination (Kieffer *et al.* 2004). The mafic rocks in the Taipusi area have ratios of $(Tb/Ta)_N > 1$ and $Nb/La < 1$ (table 1), also implying that it may have undergone significant upper crustal contamination. Ratios of Nb/U do not experience significant differentiation during the partial melting of mantle, and can thus be used to reflect geochemical characteristics of magma source region. The Nb/U ratios of mafic rocks in the Taipusi area range from 3.58 to 8.28, which are lower than that of primitive mantle (~34, Sun and McDonough 1989) and close to that of continental crust (9–12, Hofmann 1988), also suggesting that the magma underwent crustal contamination. The ratios of Nb/Ta range from 1.50 to 13.91 with an average value of 8.14, which are also distinguished from that of primitive mantle (17.39, Sun and McDonough 1989). Ratios of elements with

similar total partition coefficients would not be influenced by fractional crystallization and degree of partial melting; thus their correlation can be used to determine the existence and degree of crustal contamination. As shown in figure 11(a–d), the linear correlations of Zr *vs.* Th, Nb *vs.* Th, Nb/Ta *vs.* La/Yb and La/Nb *vs.* Zr/Nb imply that assimilation and crustal contamination occurred during the crystallization process. Moreover, the considerably varied Th and U contents as well as different $^{206}Pb/^{238}U$ ages among zircons from the diabase also indicate that some zircons originated through capture. The information of captured zircons preserved in diabase indicates the existence of an old basement in the study area. These inherited zircons may have been incorporated in the mafic magma by way of crustal assimilation and contamination when they passed through the basement.

The characteristics of source mantle should be considered when we study magma evolutionary processes. Aside from information on fractional crystallization and crustal contamination, features of original mantle magma can also be revealed by major and trace element compositions. The Zr/Hf ratios of mafic rocks in the Taipusi area range from 29.77 to 40.18 with an average value of 35.81. These values are close to the primitive mantle value (36.73, Sun and McDonough 1989) but significantly higher than that of continental crust (∼11, Weaver 1991). This implies that the magma originated from the mantle or its source was influenced by subduction metasomatic fluids. In the Th/Nb *vs.* Ce/Nb diagram (figure 11a), these samples clearly plot along the direction of subduction-derived components, which are close to arc field and far away from crustal material field. This indicates a mantle wedge magmatic source that was modified by subduction metasomatic aqueous fluids released by dehydration; and that the continental crust component played an insignificant role in the source region. In addition, a better identification of the impact of subduction metasomatic fluids and crustal sediments on source evolution is illustrated on the Ba/Zr *vs.* Th/Zr plot (figure 11b), which shows an evolutionary tendency towards altered oceanic crustal fluids. This is further reflected by the Nb/Y *vs.* La/Yb plot (figure 11c), on which most of the samples plot in the fluid-induced metamorphism field. These plots confirm that slab-derived fluids contributed significantly to the generation and evolution of the magma rather than influence from subducted sediment and the melt. Immobile elements, such as Nb, Yb and Zr, are employed to discriminate the nature of the magma source. Ratios of Nb/Yb can provide a robust indicator of mantle fertility (Pearce and Stern 2006; Xu *et al.* 2014). In the diagram of Zr/Yb *vs.* Nb/Yb (figure 11d), Nb/Yb ratios of the mafic rocks in the Taipusi area are in a range of 1.83–4.47, most of which are higher than that of N-MORB (0.76, Sun and McDonough 1989) and approach values of E-MORB (3.5, Sun and McDonough 1989), indicating that the mantle source of these rocks is probably an enriched mantle wedge altered by subduction fluids. LREE enrichment could also be a signature of enriched mantle source and suggests the involvement of enriched mantle components on the origin of these mafic rocks (Zhou *et al.* 2015). The enriched mantle is generally thought to be related to recycling of subduction crustal components (Donnelly *et al.* 2004). Source mantle features can be studied further by using plots of Ti/Yb *vs.* Nb/Yb (figure 11e) and Th/Yb *vs.* Nb/Yb (figure 11f). As shown in the diagrams, the source mantle of the mafic rocks can be identified as altered enrichment mantle related to continental arcs. Thus, we infer that source magma of the Taipusi area mafic rocks originated from an enriched mantle altered by aqueous fluids derived from the subducting plate that experienced fractional crystallization, assimilation and contamination of crustal materials to different degrees during their ascent through the lithosphere.

5.2.2 *Zircon geochemical insights*

Zircon is a host for significant fractions of U, Th, Hf, and the REE in the whole-rock abundance (O'Hara *et al.* 2001; Hoskin and Schaltegger 2003). In addition, Zr–Hf fractionation has been reported for highly evolved magmatic systems (Bau 1996). Since most Hf-enriched zircons were found in evolved rock-types, it is likely that the Hf concentration of zircon has a positive correlation with magmatic differentiation (Hoskin *et al.* 2000; Hoskin and Schaltegger 2003). Meanwhile, the fractionation of Zr and Hf in zircon-crystallizing melts may be correlated with the Zr/Hf activity coefficient ratio in the melt (Linnen and Keppler 2002). Therefore, Zr/Hf ratio can serve as an indicator of the evolutionary degree during the magmatic differentiation process. In this study, magmatic zircons from the mafic samples have high Hf concentration values,

Table 2. *U–Pb isotopic data for zircons of mafic dikes from the Taipusi area.*

Spots no.	Element content (ppm)			Isotope ratio						Apparent age (Ma)						Zircon type
	Pb	Th	U	$^{207}Pb/^{206}Pb \pm 1\sigma$		$^{207}Pb/^{235}U \pm 1\sigma$		$^{206}Pb/^{238}U \pm 1\sigma$		$^{207}Pb/^{206}Pb \pm 1\sigma$		$^{207}Pb/^{235}U \pm 1\sigma$		$^{206}Pb/^{238}U \pm 1\sigma$		
821-12-02	75	373	485	0.0590	0.0021	0.5748	0.0185	0.0706	0.0006	568	48	461	12	440	4	Magmatic
821-12-03	403	334	372	0.0616	0.0018	0.6008	0.0203	0.0707	0.0010	661	63	478	11	440	6	Magmatic
821-12-04	279	249	348	0.0597	0.0013	0.5759	0.0157	0.0700	0.0012	592	57	462	12	436	3	Magmatic
821-12-05	398	214	606	0.1497	0.0010	8.0665	0.1619	0.3908	0.0039	2343	12	2239	18	2127	18	Inherited
821-12-06	53	156	391	0.0560	0.0014	0.5423	0.0161	0.0702	0.0005	454	42	440	9	438	3	Magmatic
821-12-08	322	269	483	0.0613	0.0021	0.5905	0.0208	0.0699	0.0007	651	39	471	11	436	8	Magmatic
821-12-09	241	393	484	0.0614	0.0013	0.5937	0.0223	0.0701	0.0012	653	48	473	10	437	7	Magmatic
821-12-10	507	414	955	0.1153	0.0009	4.7979	0.0926	0.3018	0.0023	1885	14	1785	16	1700	12	Inherited
821-12-11	298	235	994	0.1145	0.0032	2.3622	0.1547	0.1496	0.0012	1872	49	1231	47	899	7	Inherited
821-12-12	306	291	1587	0.0711	0.0007	1.5094	0.0754	0.1539	0.0007	961	19	934	31	923	4	Inherited
821-12-13	355	276	547	0.0595	0.0019	0.5727	0.0167	0.0698	0.0009	586	74	460	11	435	3	Magmatic
821-12-14	533	441	705	0.1135	0.0007	6.1337	0.0688	0.3920	0.0018	1856	11	1995	10	2132	8	Inherited
821-12-15	53	225	311	0.0614	0.0025	0.6005	0.0226	0.0709	0.0008	653	83	478	14	442	5	Magmatic
821-12-18	80	396	567	0.0585	0.0017	0.5695	0.0151	0.0706	0.0011	550	65	458	10	440	6	Magmatic
826-1-01	92	396	367	0.0585	0.0012	0.5683	0.0198	0.0705	0.0012	549	44	457	12	439	4	Magmatic
826-1-02	108	341	395	0.0605	0.0020	0.5945	0.0162	0.0713	0.0012	622	77	474	10	444	8	Magmatic
826-1-03	584	675	1499	0.0962	0.0007	2.5500	0.0321	0.1922	0.0011	1552	9	1286	9	1133	6	Inherited
826-1-04	350	224	617	0.1257	0.0011	4.9811	0.0744	0.2875	0.0014	2038	15	1816	13	1629	7	Inherited
826-1-05	218	286	402	0.0585	0.0023	0.5769	0.0163	0.0715	0.0009	547	79	462	9	445	5	Magmatic
826-1-06	367	343	445	0.1258	0.0017	3.9539	0.1118	0.2279	0.0026	2040	24	1625	23	1324	14	Inherited
826-1-07	59	321	430	0.0617	0.0020	0.6022	0.0204	0.0708	0.0013	664	56	479	10	441	3	Magmatic
826-1-08	424	475	1499	0.1072	0.0011	3.4502	0.1460	0.2334	0.0036	1752	20	1516	33	1352	19	Inherited
826-1-10	660	966	1519	0.0804	0.0008	1.8418	0.0345	0.1662	0.0008	1206	23	1061	12	991	5	Inherited
826-1-11	133	265	564	0.0573	0.0017	0.5605	0.0218	0.0709	0.0009	502	62	452	11	442	3	Magmatic
826-1-12	339	419	443	0.0568	0.0011	0.5566	0.0227	0.0711	0.0010	485	38	449	10	443	6	Magmatic
826-1-13	63	215	316	0.0594	0.0013	0.5828	0.0247	0.0711	0.0009	581	44	466	14	443	5	Magmatic
826-1-14	176	236	567	0.0611	0.0012	0.5947	0.0173	0.0706	0.0008	644	40	474	10	440	8	Magmatic
826-1-15	1311	556	617	0.1098	0.0004	4.7853	0.2941	0.3162	0.0009	1796	6	1782	52	1771	5	Inherited
826-1-16	157	279	343	0.0590	0.0022	0.5706	0.0230	0.0702	0.0011	568	59	458	12	437	3	Magmatic
826-1-17	132	287	404	0.0614	0.0018	0.6010	0.0202	0.0710	0.0007	653	40	478	12	442	7	Magmatic
826-1-18	103	478	633	0.0623	0.0012	0.6081	0.0163	0.0708	0.0014	685	40	482	10	441	9	Magmatic
826-1-19	78	349	353	0.0602	0.0023	0.5843	0.0182	0.0704	0.0011	611	53	467	11	439	3	Magmatic
826-1-20	124	212	471	0.0626	0.0013	0.6105	0.0170	0.0707	0.0008	695	51	484	10	441	5	Magmatic

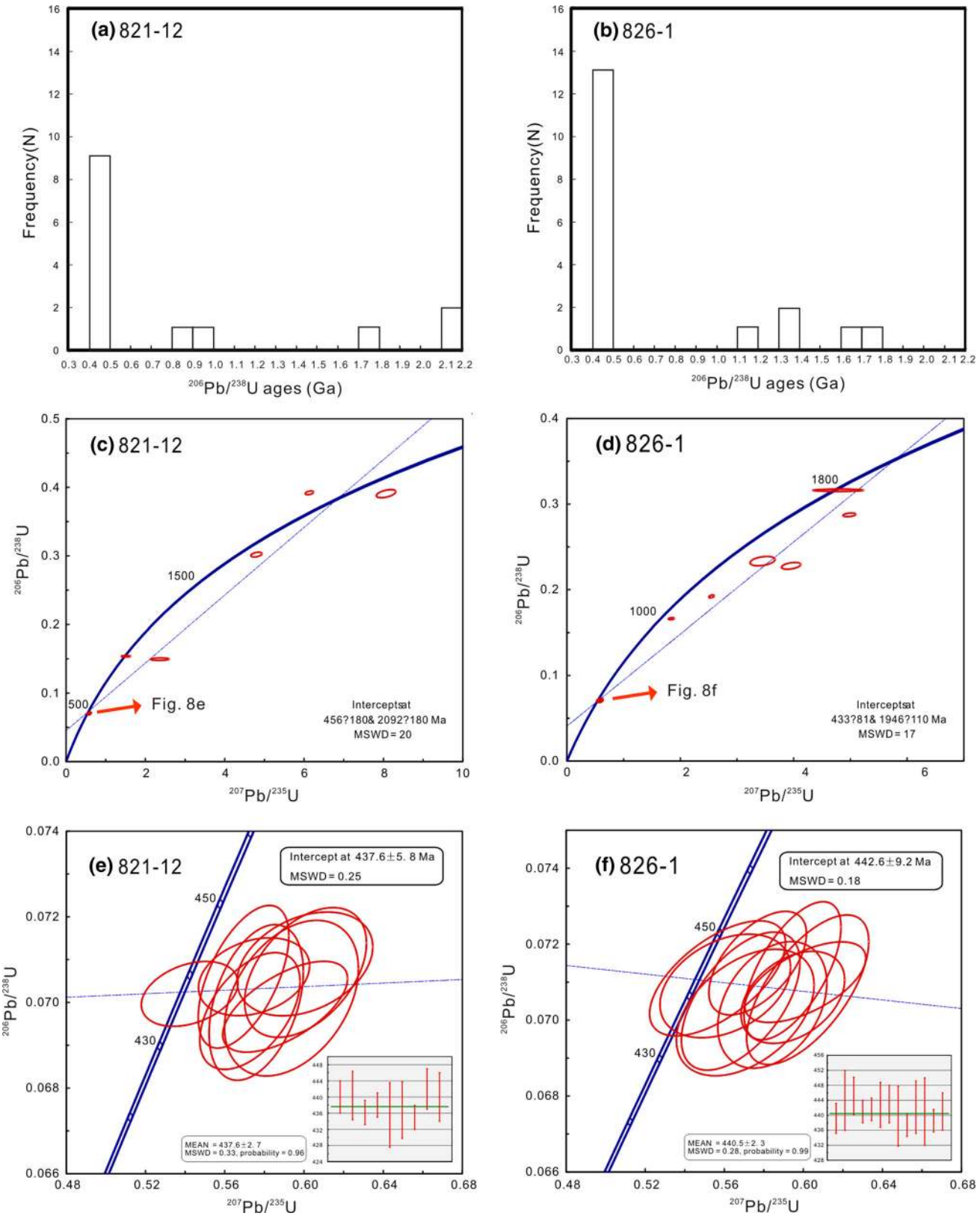

Figure 8. (**a**–**b**) Histogram of $^{206}Pb/^{238}U$ ages and (**c**–**f**) concordia diagram of La–ICP–MS zircon U–Pb dating results for the mafic rock samples 821-12 and 826-1 from the Taipusi area.

Table 3. *Trace element compositions and related calculating parameters for zircons of the mafic dikes from the Taipusi area.*

	Sample 821-12													
Spot no.	02	03	04	05	06	08	09	10	11	12	13	14	15	18
La	0.10	0.39	0.75	0.80	10.42	0.86	0.54	0.74	1.64	1.13	0.80	1.30	0.85	0.36
Ce	44.6	50.2	105.2	53.3	125.7	63.3	59.9	31.6	7.6	6.9	98.7	25.5	83.5	37.5
Pr	0.33	0.41	0.94	0.89	7.78	0.66	0.29	1.26	0.68	0.82	0.37	1.23	0.20	0.35
Nd	5.0	6.2	9.8	7.9	50.6	9.0	4.6	15.3	6.5	8.1	4.8	13.9	2.3	4.1
Sm	9.9	10.1	13.6	9.0	32.8	12.8	8.5	22.3	13.4	16.2	6.7	18.2	5.9	6.8
Eu	1.87	3.37	4.10	1.07	3.60	2.68	2.86	2.32	0.32	0.32	2.09	2.83	2.11	1.03
Gd	57	40	32	40	118	37	46	105	111	124	30	84	43	29
Tb	17	14	11	12	39	13	16	31	46	58	11	28	17	9
Dy	201	196	160	148	460	199	272	344	620	803	169	336	243	107
Ho	71	73	50	52	169	78	117	117	236	320	64	123	99	39
Er	334	416	239	248	778	411	533	504	1095	1516	340	549	501	191
Tm	67	93	59	51	159	90	109	97	227	316	75	112	106	38
Yb	698	829	618	551	1625	794	1179	964	2215	3077	679	1098	1161	425
Lu	119	182	133	97	274	162	214	152	374	504	136	187	209	72
Y	2506	2836	3221	1770	5614	2481	2766	3942	7551	10130	2565	3827	3421	2387
Ti	33	17	20	29	465	12	15	58	51	21	18	62	13	22
Hf	30807	32367	30397	30469	30098	31484	32585	27578	34171	32336	32380	22981	32700	29371
Nb	2.56	6.23	7.51	8.61	20.20	9.24	7.44	5.77	2.40	2.45	10.73	8.74	14.50	3.03
Ta	1.39	3.48	6.75	4.29	8.20	6.66	2.26	3.07	2.11	1.93	3.49	3.75	3.85	1.67
Th	373	334	249	214	156	269	393	414	235	291	276	441	225	396
U	485	372	348	606	391	483	484	955	994	1587	547	705	311	567
Th/U	0.8	0.9	0.7	0.4	0.4	0.6	0.8	0.4	0.2	0.2	0.5	0.6	0.7	0.7
Nb/Ta	1.8	1.8	1.1	2.0	2.5	1.4	3.3	1.9	1.1	1.3	3.1	2.3	3.8	1.8
ΣREE	1626	1914	1438	1272	3853	1873	2563	2388	4954	6751	1617	2580	2474	960
LREE	62	71	134	73	231	89	77	74	30	33	113	63	95	50
HREE	1564	1843	1303	1199	3622	1784	2486	2314	4924	6718	1503	2517	2379	910
LREE/HREE	0.04	0.04	0.10	0.06	0.06	0.05	0.03	0.03	0.01	0.00	0.08	0.03	0.04	0.06
Eu/Eu*	0.19	0.44	0.58	0.15	0.16	0.35	0.35	0.12	0.02	0.02	0.38	0.18	0.29	0.19
Ce/Ce*	37.4	27.5	26.5	13.7	3.3	19.7	36.9	6.3	1.8	1.7	44.6	4.5	47.9	23.6
Zircon type	Magmatic	Magmatic	Magmatic	Inherited	Magmatic	Magmatic	Magmatic	Inherited	Inherited	Inherited	Magmatic	Inherited	Magmatic	Magmatic

Table 3. *(Continued.)*

	Sample 826-1																		
Spot no.	01	02	03	04	05	06	07	08	10	11	12	13	14	15	16	17	18	19	20
La	0.57	0.67	1.67	1.52	0.62	2.26	0.82	1.00	1.46	0.47	0.46	0.91	0.58	0.79	0.74	0.36	1.14	0.43	3.42
Ce	34.5	53.2	61.2	24.7	68.6	111.2	70.3	55.2	64.5	66.9	94.3	33.3	68.3	31.9	101.0	39.6	141.5	68.4	100.9
Pr	0.85	0.38	0.82	0.78	0.92	2.06	0.51	0.68	0.83	0.70	0.78	0.65	0.47	0.32	0.55	0.78	0.67	0.80	0.99
Nd	9.1	6.5	9.8	5.4	10.2	19.8	7.3	8.6	6.8	7.6	8.3	8.4	6.0	2.4	6.1	8.4	7.9	9.6	8.9
Sm	11.9	8.7	32.6	8.2	16.0	22.6	10.6	12.8	10.3	12.4	14.7	12.0	9.2	4.9	7.4	11.4	12.5	15.3	7.5
Eu	3.57	3.86	15.02	1.26	4.60	4.81	2.85	1.80	2.11	3.71	3.92	2.61	2.63	0.39	2.32	2.93	5.28	5.48	3.55
Gd	38	47	220	39	27	105	33	71	52	48	33	54	32	31	31	35	58	38	42
Tb	14	18	56	15	9	34	12	25	17	14	12	16	11	14	11	12	17	13	12
Dy	238	284	474	189	126	417	171	298	198	187	201	203	191	204	162	235	206	186	289
Ho	99	107	139	75	64	151	66	112	67	61	80	76	67	86	51	91	78	62	83
Er	523	482	583	363	362	707	374	507	310	338	470	368	281	440	226	455	383	272	373
Tm	107	103	125	79	88	141	87	108	64	73	117	80	58	104	60	95	86	60	82
Yb	988	1065	1311	828	887	1452	840	1071	694	763	1171	882	599	1122	525	894	978	553	773
Lu	209	200	241	155	180	249	177	184	112	175	207	161	130	202	100	173	182	105	191
Y	2165	2656	4509	2422	2276	5097	2326	3522	2241	3088	2923	2681	2778	2902	2972	2391	2827	2533	2788
Ti	22	16	106	575	15	49	17	53	65	16	20	10	17	68	16	17	15	14	31
Hf	30281	29881	38167	34106	32050	27277	32429	30747	38713	29443	32645	29212	31772	38059	33132	31208	29013	31134	34215
Nb	9.49	6.21	10.59	6.30	15.05	8.30	7.16	13.60	5.69	9.86	12.20	4.40	6.02	33.48	14.05	11.09	9.42	4.70	8.51
Ta	7.19	6.40	5.69	2.73	5.80	2.69	5.04	6.43	2.74	3.83	2.66	2.19	2.83	31.36	3.68	3.40	2.52	3.02	2.83
Th	396	341	675	224	286	343	321	475	966	265	419	215	236	556	279	287	478	349	212
U	367	395	1499	617	402	445	430	1499	1519	564	443	316	567	617	343	404	633	353	471
Th/U	1.1	0.9	0.5	0.4	0.7	0.8	0.7	0.3	0.6	0.5	0.9	0.7	0.4	0.9	0.8	0.7	0.8	1.0	0.5
Nb/Ta	1.3	1.0	1.9	2.3	2.6	3.1	1.4	2.1	2.1	2.6	4.6	2.0	2.1	1.1	3.8	3.3	3.7	1.6	3.0
ΣREE	2277	2380	3270	1785	1842	3419	1851	2456	1600	1750	2414	1898	1456	2244	1284	2054	2157	1390	1970
LREE	61	73	121	42	101	163	92	80	86	92	122	58	87	41	118	63	169	100	125
HREE	2217	2306	3149	1743	1742	3256	1759	2376	1514	1658	2292	1840	1369	2203	1166	1991	1988	1290	1845
LREE/ HREE	0.03	0.03	0.04	0.02	0.06	0.05	0.05	0.03	0.06	0.06	0.05	0.03	0.06	0.02	0.10	0.03	0.09	0.08	0.07
Eu/Eu*	0.47	0.46	0.40	0.18	0.68	0.25	0.43	0.14	0.23	0.41	0.53	0.26	0.42	0.07	0.40	0.41	0.50	0.66	0.48
Ce/Ce*	9.9	25.4	12.8	5.5	18.2	11.6	26.0	15.9	14.1	23.4	30.4	10.2	30.2	15.6	37.1	13.2	39.0	21.7	13.3
Zircon type	Mag-matic	Mag-matic	Inheri-ted	Inheri-ted	Mag-matic	Inheri-ted	Mag-matic	Inheri-ted	Inheri-ted	Mag-matic	Mag-matic	Mag-matic	Mag-matic	Inheri-ted	Mag-matic	Mag-matic	Mag-matic	Mag-matic	Mag-matic

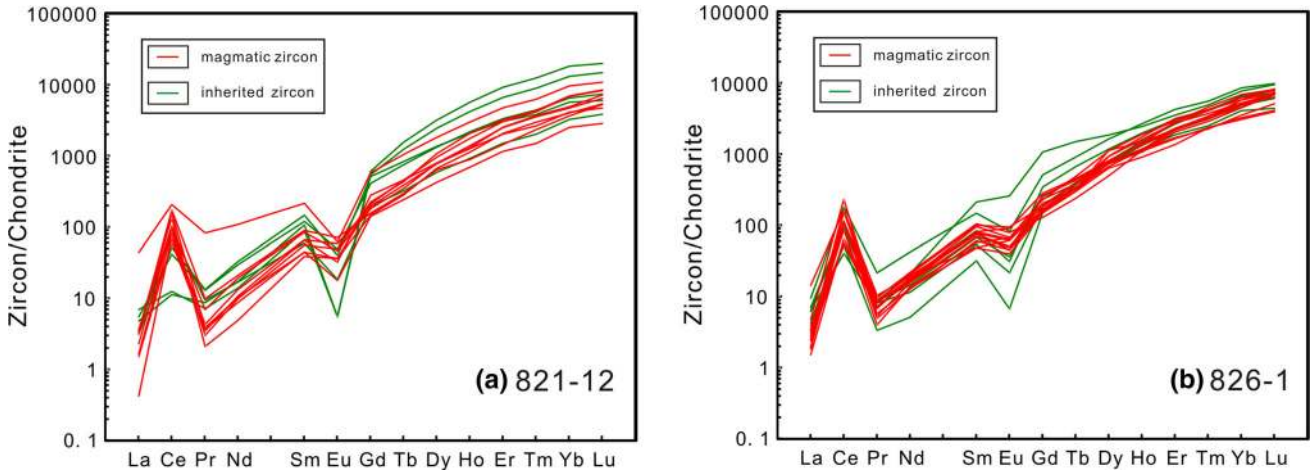

Figure 9. Chondrite-normalized REE patterns of zircons for the mafic rocks from the Taipusi area (**a**) sample 821-12 and (**b**) sample 826-1. Normalized values for chondrite are from Sun and McDonough (1989).

indicating an intensely fractionated magma origin. Moreover, zircons from highly evolved rocks are often enriched in radioactive elements such as U, Th and Pb. In zircons, U and Th can replace Zr; Th and U are positively correlated with Y and REE; and Y and Yb/Sm increase with increasing fractional crystallization. All of this reflects the evolutionary trend of magma. Highly evolved magma contains higher incompatible elements (Belousova *et al.* 2002, 2006; Li *et al.* 2014, 2017). In this study, magmatic zircons of samples 821-12 and 826-1 have high average values of U, Th, Pb and Y, suggesting that the mafic rocks at the Taipusi area were derived from a well-evolved magma.

It has been recognized that Eu may exist in +2 or +3 states in nature and its valence state is a function of temperature and oxygen fugacity of magma. As shown in table 3, all the zircons have weak negative Eu anomalies. This suggests that parental magmas may have experienced minor feldspar fractionation before zirconium saturation, or have possessed an initial negative Eu anomaly as a result of being derived from a feldspar-rich source.

A widely accepted explanation for the positive Ce anomaly in zircons is the oxidation of Ce^{3+} to Ce^{4+} during high oxygen fugacity conditions; since the ionic radius and charge of Ce^{4+} is similar to Zr^{4+}, it enters crystal lattice of zircon then replaces the latter. In contrast, the trivalent light REEs are extremely incompatible with zircon due to their differences in both charge and radius (Trail *et al.* 2011). It is also generally acknowledged that the magnitude of the Ce anomaly is controlled by oxygen fugacity of the magma, and can thus be used to provide information on the fO_2, since high fO_2 makes Ce^{3+} convert more easily to Ce^{4+} (Ballard *et al.* 2002; Claiborne *et al.* 2010; Han *et al.* 2013). As shown in table 3, most magmatic zircons have pronounced positive Ce anomalies, implying that the parent magma of the mafic rocks in the Taipusi area once had a medium to high fO_2 during its evolutionary or ascension process. In addition, Ta can easily oxidize into 5+ valence state while Nb remains in 4+ valance state, which contributes to high Nb/Ta ratios in zircons that formed in an oxidizing environment. The Nb/Ta ratios of magmatic zircons from samples 821-12 and 826-1 varies from 0.97 to 4.58 with a relatively high mean value of 2.43, also implying they were derived from an oxidizing environment.

Grimes *et al.* (2007) suggests an efficient way to identify zircon crystallization environment using U/Yb–Hf and U/Yb–Y diagrams. As shown in figure 12, these magmatic zircons mainly fall into the transitional field of oceanic crust and continental fields, implying the source of magma was metasomatized by slab fluids derived from subducted oceanic slabs.

Thus, trace element analysis indicates that the magma source was associated with the southward subduction of oceanic slabs and underwent fractional crystallization and crustal contamination to different degrees during its ascent through the lithosphere, forming mafic rocks of diversified types.

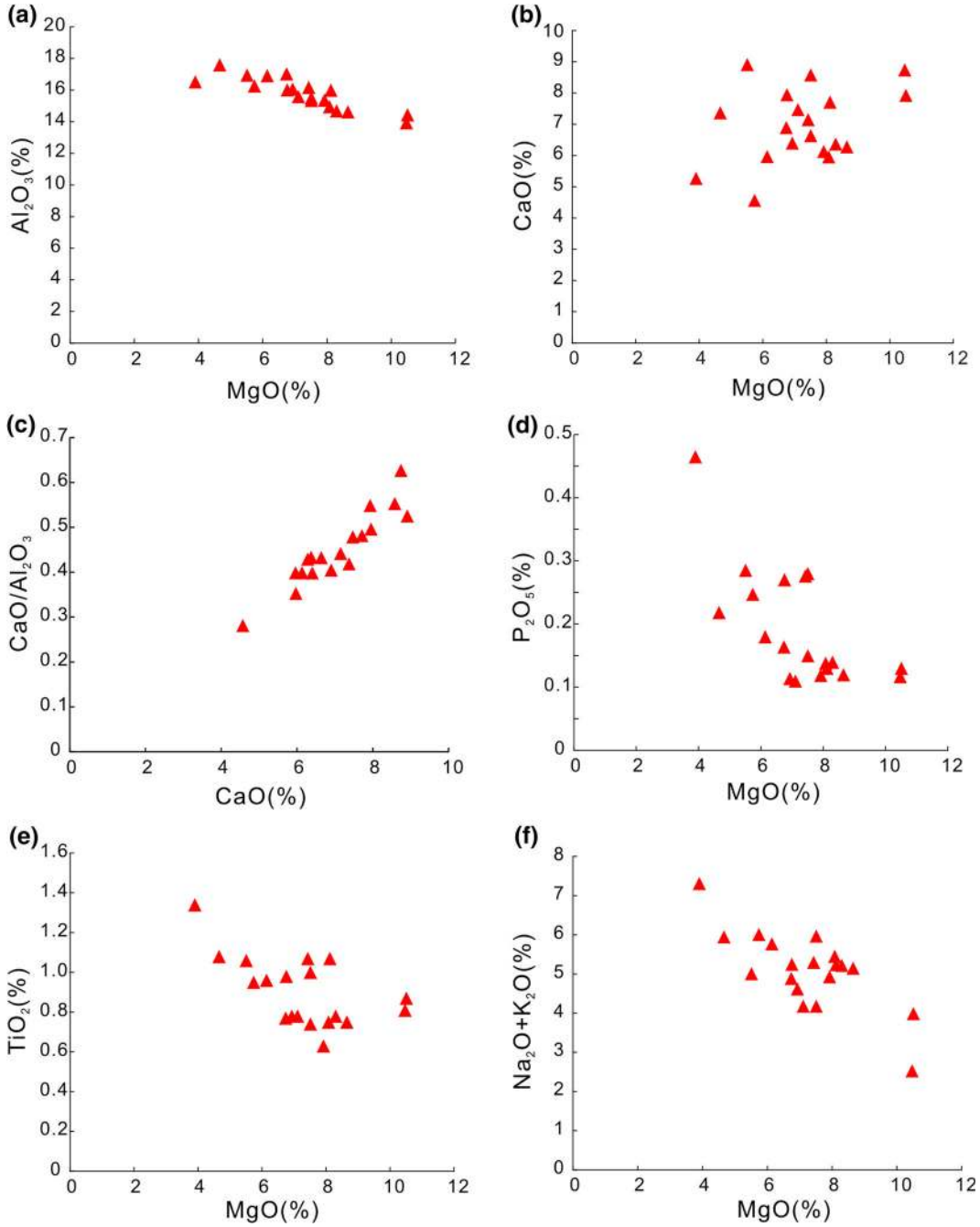

Figure 10. Discrimination diagrams of magma fractional crystallization for the mafic rocks from the Taipusi area. (**a**) MgO *vs.* Al_2O_3; (**b**) MgO *vs.* CaO; (**c**) CaO *vs.* CaO/Al_2O_3; (**d**) MgO *vs.* P_2O_5; (**e**) MgO *vs.* TiO_2 and (**f**) MgO *vs.* $Na_2O + K_2O$.

5.3 *Tectonic setting*

The major element analytical results show that the mafic rocks in the Taipusi area belong to the high-K calc-alkaline series. The average content of Al_2O_3 is 15.75%, which have similar values to continental high-alumina basalt. The TiO_2 content is similar to that of volcanic arc basalt. The enrichment of LILE and depletion of HFSE are consistent with the characteristics of volcanic arc rocks (Eiler *et al.* 2000; Grove *et al.* 2003; Li *et al.* 2013, 2016).

Furthermore, volcanic arc basalts can be subdivided into oceanic and continental types. Pearce (1983) pointed out that most basalts from active continental margins have Ta/Yb values >0.1 whereas basalts from oceanic arcs have values <0.1. The mafic rocks from the Taipusi area have Ta/Yb values ranging from 0.15 to 1.47,

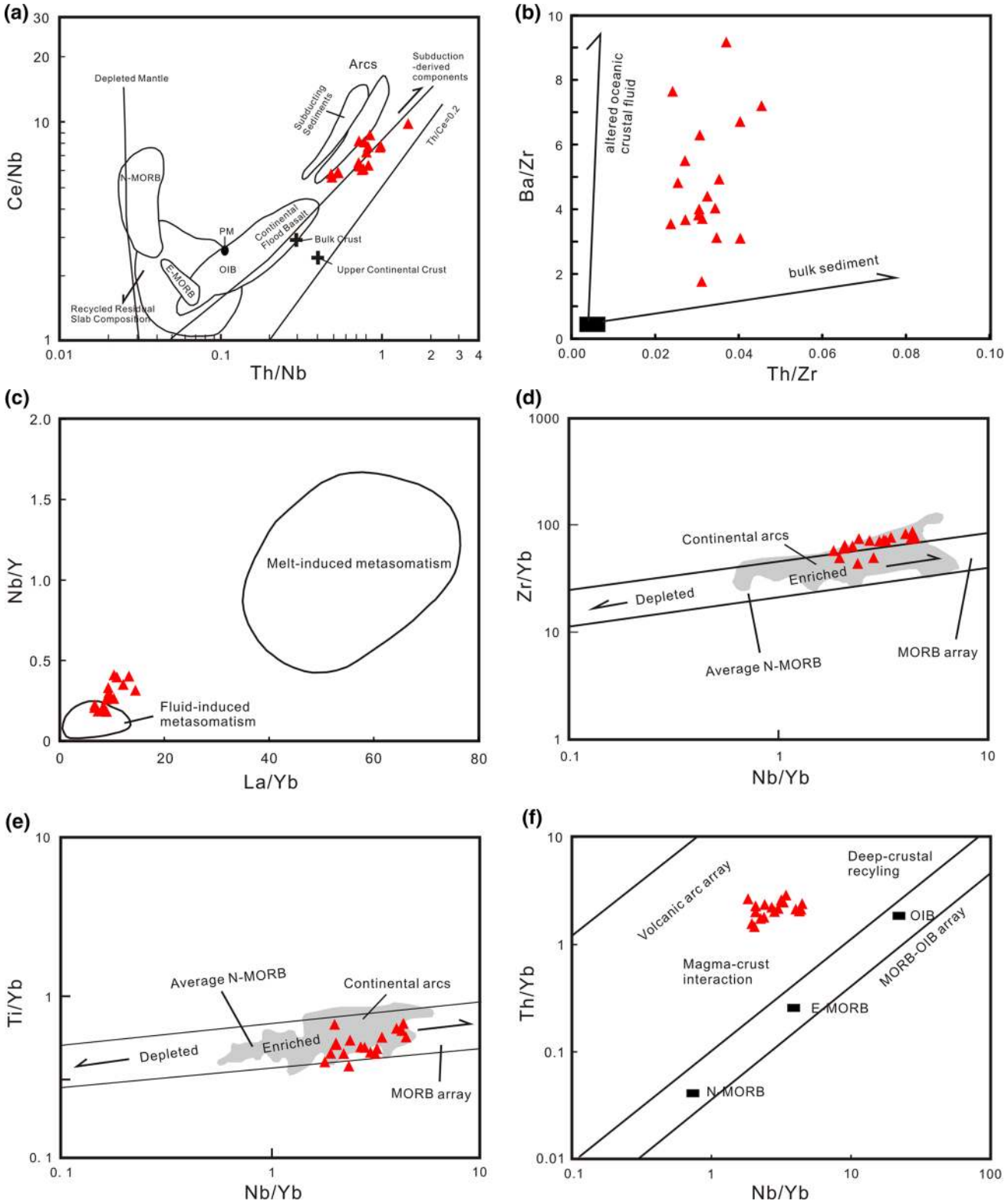

Figure 11. Discrimination diagrams of magma genesis and evolutionary process for the mafic rocks from the Taipusi area. (**a**) Th/Nb *vs.* Ce/Nb diagram (after Song *et al.* 2004); (**b**) Th/Zr *vs.* Ba/Zr diagram (after Hoffer *et al.* 2008); (**c**) La/Yb *vs.* Nb/Y diagram (after Ishizuka *et al.* 2003); (**d**) Nb/Yb *vs.* Zr/Yb diagram; (**e**) Nb/Yb *vs.* Ti/Yb diagram; (**f**) Nb/Yb *vs.* Th/Yb diagram (d), (e), and (f) after Pearce and Peate (1995).

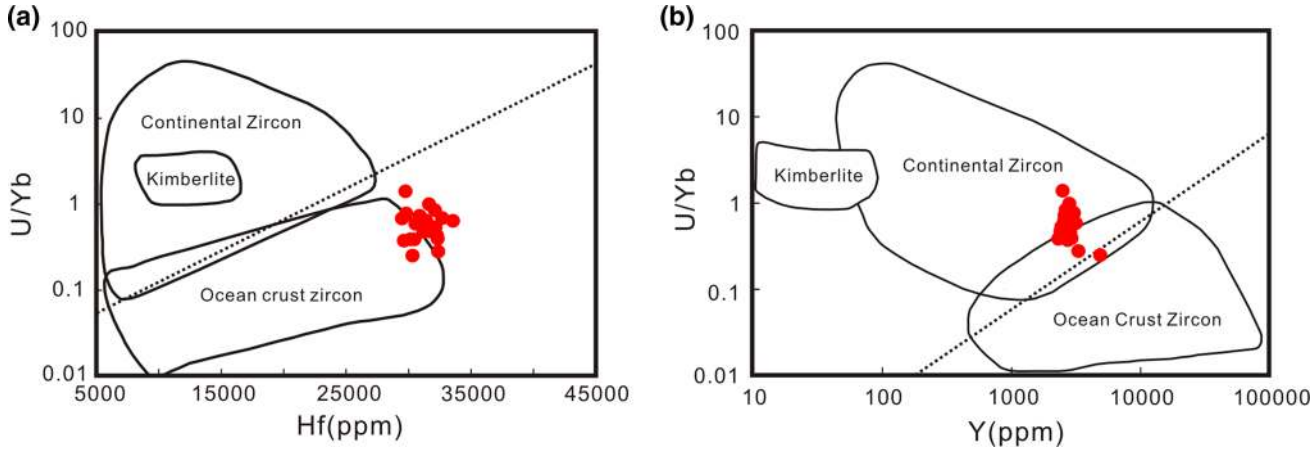

Figure 12. Discrimination diagrams of zircon crystallization environment for the mafic rocks from the Taipusi area. (**a**) U/Yb *vs.* Hf diagram and (**b**) U/Yb *vs.* Y diagram (after Grimes *et al.* 2009).

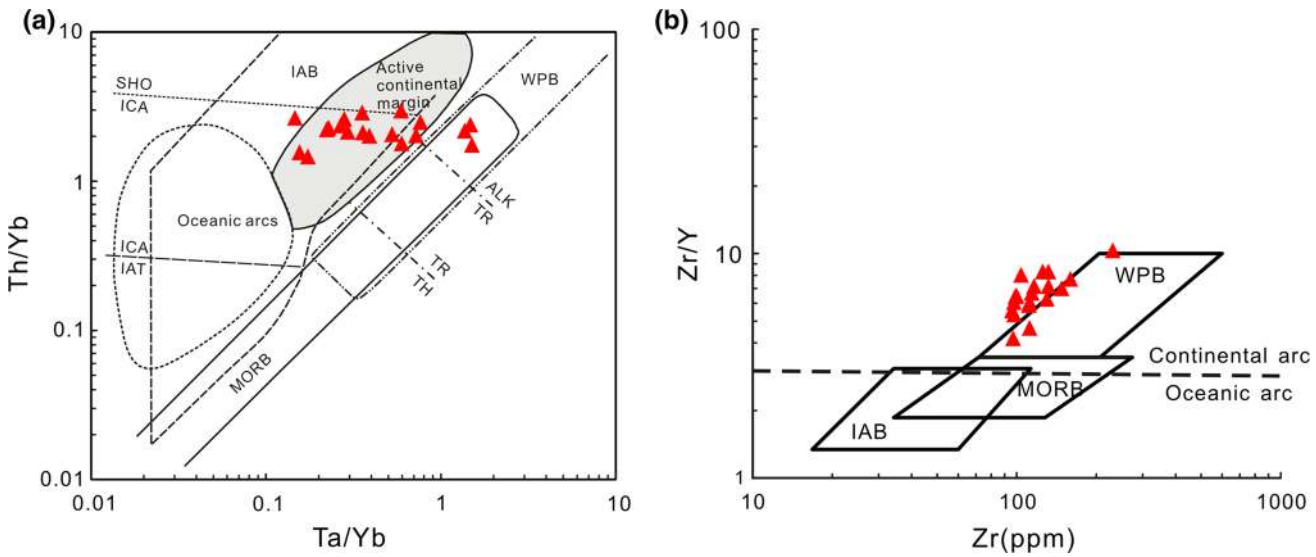

Figure 13. Discrimination diagrams of tectonic settings for the mafic rocks from the Taipusi area. (**a**) Ta/Yb *vs.* Th/Yb diagram (after Pearce 1982) and (**b**) Zr *vs.* Zr/Y diagram (after Pearce and Norry 1979 and Pearce 1983) IAB: Island arc basalt; IAT: Island arc tholeiite; ICA: Island calc-alkaline; SHO: Shoshonite; WPB: Within plate basalt; MORB: Mid-ocean ridge basalt; TH: Tholeiitic basalt; TR: Transitional basalt; ALK: Alkalic basalt.

which suggests a continental type arc environment (figure 13a). A more effective discrimination diagram for this purpose is the Zr/Y *vs.* Zr diagram of Pearce (1983) presented in figure 13(b). The mafic rocks plot in the continental margin field, which essentially favors a continental arc origin.

There is additional evidence from elemental geochemistry pointing to a continental arc origin. The enrichment of LREE and inclined-LREE with flat-HREE patterns are comparable with features of continental margin volcanic arc basalt, which are distinct from the normal mid-ocean ridge basalt and oceanic island basalt. Some elemental anomalies (such as K*, Nb* and Sr*) can be used to determine tectonic setting and related evolutionary processes of magma (Xia *et al.* 2007). Basalts with K* values higher than 1 could have originated from the island arc region and have close relationship with subduction (Nakamura *et al.* 1985). Mafic magmas contaminated by crustal materials or granitic rocks would have Nb* values lower than 1. Sr* values <1 may be deemed as results of fractional crystallization of plagioclase or metasomatic alteration of fluids (Pin *et al.* 1988). For the mafic rocks in the Taipusi area, samples have values of K*>1, Nb*<1 and Sr*>1 (table 1), indicating that the magma was derived from the mantle beneath a continental island arc that was strongly affected by subduction, then contaminated by crustal or

granitic materials with some degree of fractional crystallization.

The northern margin of NCC was strongly influenced by subduction of the Paleo-Asian ocean during the early Paleozoic to Triassic. The ca. 437 Ma mafic rocks in the Taipusi area reported in this study indicate that the middle part of the northern margin of NCC experienced subduction. These mafic rocks were formed under a subduction setting associated with enriched mantle wedge metasomatized by fluids from the subduction zone. The variable compositions of major and trace elements might be a reflection of a heterogeneous source composition, probably related to a subduction-modified sublithospheric mantle (Yang *et al.* 2014). This subduction process might have enriched the subcontinental mantle lithosphere.

In summary, the mafic rocks in the Taipusi area provide evidence of formation in a subduction environment. The mafic rocks in the Taipusi area inherited the features of continental arc rocks, and the mantle source was probably metasomatized by slab fluids with minor melts derived from either subducted oceanic slabs or pelagic sediments.

5.4 *Implications for tectonic evolution of BAB*

After the eastern landmass collided with the western landmass to form a single continental plate at ∼1.85 Ga, the NCC experienced a long period of steady tectonic evolution with a passive continental margin until the Early Cambrian (Wilde *et al.* 2002; Zhai and Santosh 2011). Afterward, the Early Paleozoic southward subduction of the Paleo-Asian ocean changed the northern margin of NCC into active continental margin. Previous studies indicate that magmatic activity related to this subduction in BAB was sustained about 80 Ma from the Cambrian (∼500 Ma) to the Middle–Late Silurian (∼420 Ma) and peaked at Late Ordovician (Wang *et al.* 2012). However, different tectonic evolution models are applied to explain the closure process of the PAO, which mainly involves the long-term continuous subduction and the north-south differential subduction. Based on different models, the late Paleozoic magmatic activity in BAB may be related to island arc subduction or collisional orogenic tectonic setting.

Previous studies on the magmatic rocks in adjacent areas may offer further understanding for the tectonic evolution of BAB. Located to the north of BAB, the Ondor Sum Subduction-Accretionary Complex Belt developed a set of complexes formed by the subduction zone, which is composed of the Ondor Sum group, Deyeqimiao plagioclase amphibolite, ultramafic rocks and oligoclase granite. It is a subduction remnant of the PAO plate and a product of island arc magmatism. The Ondor Sum group is divided into the lower Sanda and upper Halhada formation, and is a set of accretionary complexes consisting of oceanic crust and intra-oceanic arc with different ages and genesis. Jong *et al.* (2006) reported a phengite ^{40}Ar–^{39}Ar age of ∼450 Ma for the mylonite from the Halhada formation at the northern Ulan Arc, which is interpreted as the result of high-pressure metamorphism during subduction. Furthermore, Jian *et al.* (2008) obtained an age of 479.6±2.4 Ma from metamorphic gabbro cutting through the greenschist in the Tulinkai area. Consequently, it is considered that the Ondor Sum formation may have formed between late Cambrian and middle Silurian. The Deyangmiao plagioclase amphibolite is also related to the Ondor Sum subduction zone, which is the oceanic island arc that is formed by asthenospheric convection after oceanic-oceanic collision. Recently, Wang *et al.* (2015) gave a new zircon U–Pb age of 490.3±4.6 Ma of amphibolite series in eastern Ondor Sum area. Moreover, Liu *et al.* (2003) found a set of adakite rocks including quartz diorite, trondhjemite, anorthosite and dacite in the Tulinkai area and considered them as the mark of the early Paleozoic magmatic rocks resulting from subduction in this area. Geochronological results show that the earliest rock emplaced was the quartz diorite (∼467 Ma), followed by a high-grade metamorphism event and partial melting process. The dacite and trondhjemite intruded at ∼459 and ∼451 Ma respectively; and finally the anorthosite dike was formed at ∼429 Ma. In contrast, the ages of quartz diorite, dacite and anorthosite given by Jian *et al.* (2008) are 453.7±3.1, 457.9±2.6 and 425.3±2.2 Ma, respectively, indicating that the Ondor Sum–Tulinkai oceanic crust experienced ∼30 Ma subduction during the early Paleozoic period. According to chronological data, the SOB could have developed two subduction zones between 453 and 425 Ma. The northern zone may represent the subduction zone of the intra-oceanic arc, and the southern zone may represent the subduction zone of the BAB. This suggests that the southern subduction of the PAO along the BAB from the early Ordovician to the middle Silurian led to intense

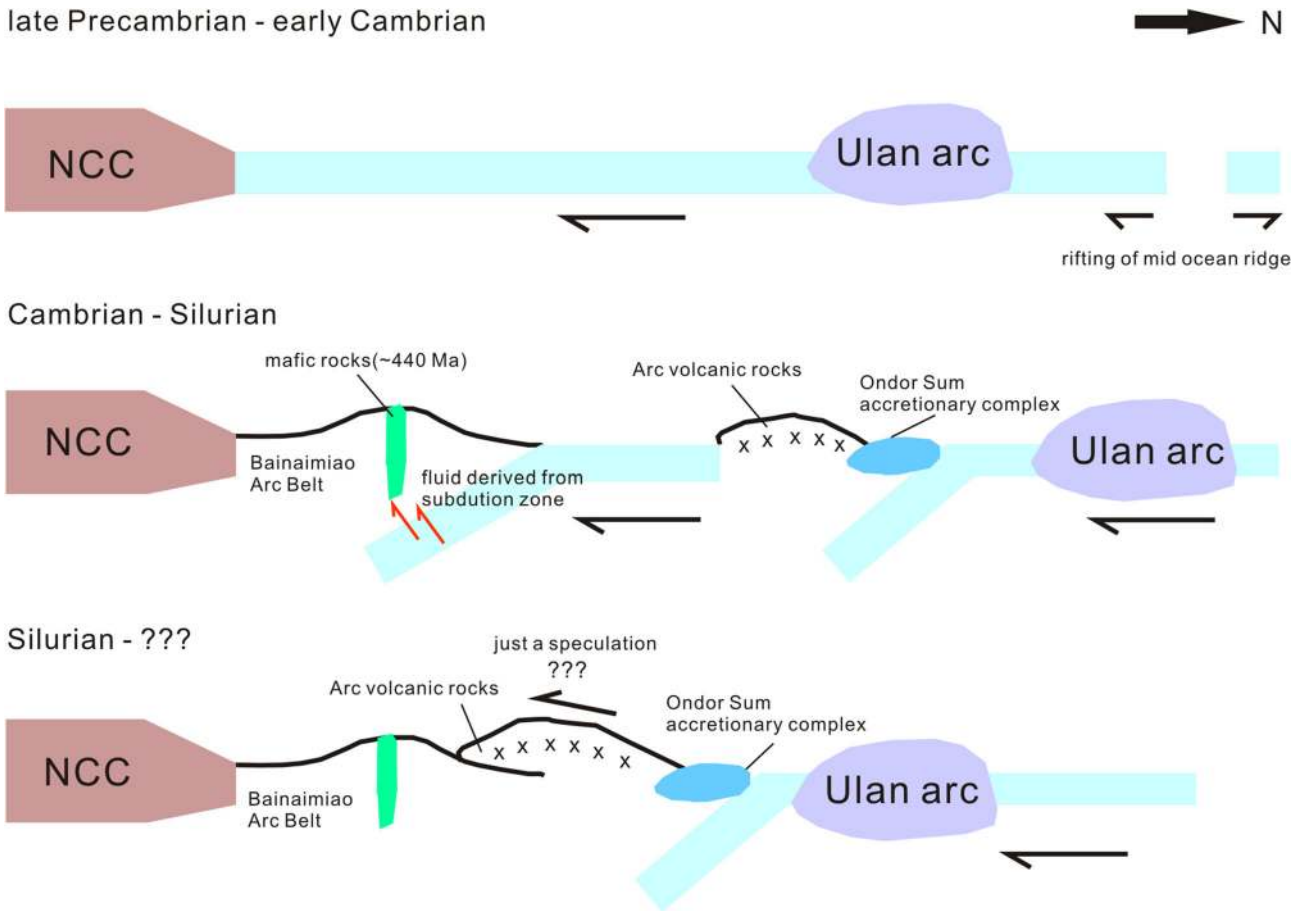

Figure 14. Cartoon-like profiles demonstrating the tectonic evolution of the Bainaimiao arc belt.

volcanic activity and the formation of widely distributed volcanic rocks in the northern margin of NCC.

The BAB has been recognized as an island arc by several authors (e.g., Tang and Yan 1993; Zhang *et al.* 2014). Correspondingly, the northern margin of NCC was considered as a passive continental margin on account of widely developed epicontinental sea sedimentation from the Cambrian to the middle Ordovician (Zhang *et al.* 2006). In addition, Zhang *et al.* (2014) proposed that the BAB is an ensialic island arc characterized by a different evolution history and basement compositions from the northern NCC. They also suggested that a South Bainaimiao Ocean existed between BAB and NCC during the Cambrian–Ordovician period. Long-term northward subduction brought about closure of the South Bainaimiao Ocean from the Early Cambrian to Middle Silurian (0.52–0.42 Ga) and final accretion of the Bainaimiao island arc to North China Craton during the Late Silurian to early Devonian by arc-continent collision. In comparison, the high initial strontium isotope ratio ($^{87}Sr/^{86}Sr_i$=0.7146) of granites (Shao 1989) and the εNd value of 2.4±1.7 of granodiorite (Nie and Bjørlykke 1999) imply that the BAB formed by magma mixing between mantle-derived components and crustal rocks in an active continental Cordilleran–type margin rather than in an island arc (Xiao *et al.* 2003). Moreover, according to detailed geochronology and geochemistry of Bainaimiao metamorphic volcanic rocks, Liu *et al.* (2014) believed that the original magma of these rocks may have been derived from enriched mantle wedge and metasomatized by fluid during subduction and hybridized by continental crust materials, with active continental margin features.

Within the middle part of BAB, these mafic dikes from the Taipusi area have similar geochemical features with the Bainaimiao metavolcanic rocks, implying a similar source region and tectonic setting. Additionally, mafic dikes in the Taipusi area are dated at ~440 Ma, which is also consistent with the peak magmatic activity of Bainaimiao Arc Belt during the Late Ordovician. The geochemical features of these Taipusi area mafic dikes suggest

the tectonic environment of BAB to be a continental arc rather than an island arc. Hence, we conclude that the middle section of Bainaimiao Arc Belt once underwent intensive continental accretion caused by southward subduction of the Paleo-Asian ocean during the Early Paleozoic.

Consequently, the early Paleozoic tectonic evolution of the northern margin of NCC can be summarized as follows (figure 14): During the period from the late Precambrian to early Cambrian, the mid-ocean ridge of PAO gradually expanded and formed the Ondor Sum serpentinite that later migrated from the north to the south with the oceanic plate. Meanwhile, the Bainaimiao area continued to suffer from compression and stress accumulation. From Cambrian to Silurian, ocean–ocean subduction occurred on the south side of the Ondor Sum serpentinite, which resulted in an accretionary complex and arc volcanic rocks. At the same time, the northern margin of NCC was converted into an active continental margin, and the oceanic crust subducted under the continental crust. The metasomatism from subduction resulted in the formation of the mafic rocks in the Taipusi area.

6. Conclusion

- Zircon LA–ICP–MS U–Pb concordant ages of the mafic rocks in the Taipusi area are 437–442 Ma, consistent with the peak magmatism at the Bainaimiao Arc Belt. This indicates that formation of these mafic rocks is associated with the Paleo-Asian Ocean southward subduction during Early Paleozoic.
- The magma of the mafic rocks originated from an altered enriched mantle that was probably metasomatized by subducting slab fluids, and underwent notable fractional crystallization and crustal contamination during their ascent through the lithosphere under an active continental arc setting.
- The middle section of Bainaimaio Arc Belt is a continental arc rather than an island arc during the early Silurian. No island arcs were generated and accreted to the northern North China Craton during late Devonian to early Silurian.

Acknowledgements

This work was co-financed by the Fundamental Research Funds for the Central Universities, China University of Geosciences (Wuhan) (Grant No. CUG150612) and the National Natural Science Foundation of China (Grant No. 41502067). The authors thank anonymous reviewers for their detailed and valuable comments that greatly improved the manuscript.

References

Andersen T 2002 Correction of common lead in U–Pb analyses that do not report ^{204}Pb; *Chem. Geol.* **192(1–2)** 59–79.

Ballard J R, Palin J M and Campbell I H 2002 Relative oxidation states of magmas inferred from Ce (IV)/Ce (III) in zircon: Application to porphyry copper deposits of northern Chile; *Contrib. Mineral. Petrol.* **144(3)** 347–364.

Bau M 1996 Controls on the fractionation of isovalent trace elements in magmatic and aqueous systems: Evidence from Y/Ho, Zr/Hf, and lanthanide tetrad effect; *Contrib. Mineral. Petrol.* **123(3)** 323–333.

Belousova E A, Griffin W L, O'Reilly S Y and Fisher N I 2002 Igneous zircon: Trace element composition as an indicator of source rock type; *Contrib. Mineral. Petrol.* **143(5)** 602–622.

Belousova E A, Griffin W L and O'Reilly S Y 2006 Zircon crystal morphology, trace element signatures and Hf isotope composition as a tool for petrogenetic modelling: Examples from eastern Australian granitoids; *J. Petrol.* **47(2)** 329–353.

Chen B, Jahn B M, Wilde S and Xu B 2000 Two contrasting Paleozoic magmatic belts in northern Inner Mongolia, China: Petrogenesis and tectonic implications; *Tectonophys.* **328(1)** 157–182.

Chen B, Jahn B M and Tian W 2009 Evolution of the Solonker suture zone: Constraints from zircon U–Pb ages, Hf isotopic ratios and whole-rock Nd–Sr isotope compositions of subduction- and collision-related magmas and forearc sediments; *J. Asian Earth Sci.* **34(3)** 245–257.

Claiborne L L, Miller C F and Wooden J L 2010 Trace element composition of igneous zircon: A thermal and compositional record of the accumulation and evolution of a large silicic batholith, Spirit Mountain, Nevada; *Contrib. Mineral. Petrol.* **160(4)** 511–531.

Cope T, Ritts B, Darby B, Fildani A and Graham S 2005 Late Paleozoic sedimentation on the northern margin of the North China block: Implications for regional tectonics and climate change; *Int. Geol. Rev.* **47(3)** 270–296.

Donnelly K E, Goldstein S L, Langmuir C H and Spiegelman M 2004 Origin of enriched ocean ridge basalts and implications for mantle dynamics; *Earth Planet. Sci. Lett.* **226(3–4)** 347–366.

Eiler J M, Grawford A, Elliott T, Farley K A, Valley J W and Stolper E M 2000 Oxygen isotope geochemistry of oceanic arc lavas; *J. Petrol.* **41(2)** 229–256.

Feng X X, Yao S Z, Wang J S, Wei J L, Li G Y, Wang J Y and Feng X B 2014 LA–MC–ICP–MS zircon U–Pb dating of the pluton in the Bainaimiao Cu–Mo deposit of Inner Mongolia and its geological significance; *Geol. Explor.* **18(2)** 179–197 (in Chinese with English abstract).

Grimes C B, John B E, Kelemen P B, Mazdab F, Wooden J L, Cheadle M J, Hanghoj K and Schwartz J J 2007 The trace element chemistry of zircons from oceanic crust: A method for distinguishing detrital zircon provenance; *Geology* **35(7)** 643–646.

Grimes C B, John B E, Cheadle M J, Mazdab F K, Wooden J L, Swapp S and Schwartz J J 2009 On the occurrence, trace element geochemistry, and crystallization history of zircon from *in situ* ocean lithosphere; *Contrib. Mineral. Petrol.* **158(6)** 757–783.

Grove T L, Elkins-Tanton L T, Parman S W, Chatterjee N, Müntener O and Gaetani G A 2003 Fractional crystallization and mantle melting controls on calc-alkaline differentiation trends; *Contrib. Mineral. Petrol.* **145(5)** 515–533.

Han Y G, Zhang S H, Pirajno F, Zhou X W, Zhao G C, Qü W J, Liu S H, Zhang J M, Liang H B and Yang K 2013 U–Pb and Re–Os isotopic systematics and zircon Ce^{4+}/Ce^{3+} ratios in the Shiyaogou Mo deposit in eastern Qinling, central China: Insights into the oxidation state of granitoids and Mo (Au) mineralization; *Ore Geol. Rev.* **55(15)** 29–47.

Hey M H 1982 The determination of ferrous and ferric iron in rocks and minerals and a note on sulphosalicylic acid as a reagent for Fe and Ti; *Mineral. Mag.* **46(341)** 111–118.

Hoffer G, Eissen J P, Beate B, Bourdon E, Fornari M and Cotton J 2008 Geochemical and petrological constraints on rear-arc magma genesis processes in Ecuador: The Puyo cones and Mera lavas volcanic formations; *J. Volcanol. Geotherm. Res.* **176(1)** 107–118.

Hofmann A W 1988 Chemical differentiation of the Earth: The relationship between mantle, continental crust, and oceanic crust; *Earth Planet. Sci. Lett.* **90(3)** 297–314.

Hoskin P W O, Kinny P D, Wyborn D and Chappell B W 2000 Identifying accessory mineral saturation during differentiation in granitoid magmas: An integrated approach; *J. Petrol.* **41(9)** 1365–1396.

Hoskin P W O and Schaltegger U 2003 The composition of zircon and igneous and metamorphic petrogenesis; *Rev. Mineral. Geochem.* **53(1)** 27–62.

Hoskin P W O 2005 Trace-element composition of hydrothermal zircon and the alteration of Hadean zircon from the Jack Hills, Australia; *Geochim. Cosmochim. Acta* **69(3)** 637–648.

Irvine T N and Baragar W R A 1971 A guide to the chemical classification of the common volcanic rocks; *Can. J. Earth Sci.* **8(5)** 523–548.

Ishizuka O, Taylor R N, Milton J A and Nesbitt R W 2003 Fluid–mantle interaction in an intra-oceanic arc: Constraints from high-precision Pb isotopes; *Earth Planet. Sci. Lett.* **211(3–4)** 221–236.

Jahn B M 2004 The Central Asian Orogenic Belt and growth of the continental crust in the Phanerozoic; *Geol. Soc. Lond. Spec. Publ.* **226(1)** 73–100.

Jesus A P, Mateus A, Munhá J M and Tassinari C 2014 Internal architecture and Fe–Ti–V oxide ore genesis in a Variscan synorogenic layered mafic intrusion the Beja Layered Gabbroic Sequence (Portugal); *Lithos* **190–191(3)** 111–136.

Jian P, Liu D, Kröner A, Windley B F, Shi Y, Zhang F, Shi G, Miao L, Zhang W, Zhang L and Ren J 2008 Time scale of an early to mid-Paleozoic orogenic cycle of the long-lived Central Asian Orogenic Belt, Inner Mongolia of China: Implications for continental growth; *Lithos* **101(3–4)** 233–259.

Jian P, Liu D and Kröner A 2010 Evolution of a Permian intraoceanic arc-trench system in the Solonker suture zone, Central Asian Orogenic Belt, China and Mongolia; *Lithos* **118(1–2)** 169–190.

Jong K D, Xiao W, Windley B F, Masago H and Lo C H 2006 Ordovician $^{40}Ar/^{39}Ar$ phengite ages from the blueschist-facies Ondor Sum subduction–accretion complex (Inner Mongolia) and implications for the early Paleozoic history of continental blocks in China and adjacent areas; *Am. J. Sci.* **106(10)** 799–845.

Khain E V, Bibikova E V, Salnikova E B, Kröner A, Gibsher A S, Didenko A N, Degtyarev K E and Fedotova A A 2003 The Palaeo-Asian Ocean in the Neoproterozoic and early Palaeozoic: New geochronologic data and palaeotectonic reconstructions; *Precamb. Res.* **122(1)** 329–358.

Kieffer B, Arndt N, Lapierre H, Bastien F, Bosch D, Pecher A, Yirgu G, Ayalew D, Weis D, Jerram D A, Keller F and Meugniot C 2004 Flood and shield basalts from Ethiopia: Magmas from the African Superswell; *J. Petrol.* **45(4)** 793–834.

Li H, Watanabe K, Xi X S and Yonezu K 2013 Geochemistry of volcanic rocks at Zhaokalong iron-copper polymetallic ore deposit, Qinghai Province, China: Implications for the tectonic background; *Proc. Earth Planet. Sci.* **6** 58–63.

Li H, Watanabe K and Yonezu K 2014 Zircon morphology, geochronology and trace element geochemistry of the granites from the Huangshaping polymetallic deposit, South China: Implications for the magmatic evolution and mineralization processes; *Ore Geol. Rev.* **60** 14–35.

Li H, Xi X S, Sun H S, Kong H, Wu Q H, Wu C M and Gabo-Ratio J A S 2016 Geochemistry of the Batang Group in the Zhaokalong area, Yushu, Qinghai: Implications for the Late Triassic tectonism in the northern Sanjiang region, China; *Acta Geol. Sin.-Engl. Ed.* **90(2)** 704–721.

Li H, Sun H S, Wu J H, Evans N J, Xi X S, Peng N L, Cao J Y and Gabo-Ratio J A S 2017 Re–Os and U–Pb geochronology of the Shazigou Mo polymetallic ore field, Inner Mongolia: Implications for Permian–Triassic mineralization at the northern margin of the North China Craton; *Ore Geol. Rev.* **83** 287–299.

Li J F, Zhang Z C and Han B F 2010 Ar-Ar and zircon SHRIMP geochronology of hornblendite and diorite in northern Darhan Muminggan Joint Banner, Inner Mongolia, and its geological significance; *Acta Petrol. Mineral.* **29(6)** 732–740.

Li Y L, Zhou H W, Xiao W J, Zhong Z Q and Yin S P 2012a Superposition of Paleo-Asian and West-Pacific tectonic domains in the eastern section of the Solonker Suture Zone: Insights from petrology, geochemistry and geochronology of deformed diorite in Xar Moron Fault Zone, Inner Mongolia; *J. China Univ. Geosci.* **37(3)** 433–450.

Li W, Zhong R, Xu C, Song B and Qu W 2012b U–Pb and Re–Os geochronology of the Bainaimiao Cu–Mo–Au deposit, on the northern margin of the North China Craton, Central Asia Orogenic Belt: Implications for ore genesis and geodynamic setting; *Ore Geol. Rev.* **48** 139–150.

Li W B, Hu C S, Zhong R C and Zhu F 2015 U–Pb, $^{39}Ar/^{40}Ar$ geochronology of the metamorphosed volcanic rocks of the Bainaimiao Group in central Inner Mongolia and its implications for ore genesis and geodynamic setting; *J. Asian Earth Sci.* **97** 251–259.

Linnen R L and Keppler H 2002 Melt composition control of Zr/Hf fractionation in magmatic processes; *Geochim. Cosmochim. Acta* **66(18)** 3293–3301.

Liu C F, Liu W C, Wang H P, Zhou Z, Zhang H and Tang Y 2014 Geochronology and Geochemistry of the Bainaimiao Metavolcanic Rocks in the Northern Margin of North China Craton; *Acta Geol. Sin.* **88(7)** 1273–1287 (in Chinese with English abstract).

Liu D, Jian P, Zhang Q, Zhang F, Shi Y, Shi G, Zhang N and Tao H 2003 SHRIMP dating of adakites in the Tulingkai Ophiolite, Inner Mongolia: Evidence for the early Paleozoic subduction; *Acta Geol.* **77(3)** 317–327 (in Chinese with English abstract).

Liu Y S, Hu Z C, Gao S, Günther D, Xu J, Gao C and Chen H 2008 *In situ* analysis of major and trace elements of anhydrous minerals by LA-ICP-MS without applying an internal standard; *Chem. Geol.* **257(1–2)** 34–43.

Liu Y S, Gao S, Hu Z C, Gao C G, Zong K Q and Wang D 2010 Continental and oceanic crust recycling-induced melt-peridotite interactions in the Trans-North China Orogen: U–Pb dating, Hf isotopes and trace elements in zircons of mantle xenoliths; *J. Petrol.* **51(1–2)** 537–571.

Miao L C, Fan W M, Liu D Y, Zhang F, Shi Y and Guo F 2008 Geochronology and geochemistry of the Hegenshan ophiolitic complex: Implications for late stage tectonic evolution of the Inner Mongolia–Daxinganling Orogenic Belt; *China J. Asian Earth Sci.* **32(5–6)** 348–370.

Nakamura E, Campbell I H and Sun S S 1985 The influence of subduction processes on the geochemistry of Japanese alkaline basalts; *Nature* **316** 55–58.

Nie F and Bjørlykke A 1999 Nd and Sr isotope constraints on the age and origin of Proterozoic metamafic volcanic rocks in the Bainaimiao–Wenduermiao district, south-central Inner Mongolia, China; *Cont. Dyn.* **4(1)** 1–14.

O'Hara M J, Fry N and Prichard H M 2001 Minor phases as carriers of trace elements in non-modal crystal–liquid separation processes II: Illustrations and bearing on behavior of REE, U, Th and the PGE in igneous processes; *J. Petrol.* **42(10)** 1887–1910.

Pearce J A and Norry M J 1979 Petrogenetic implications of Ti, Zr, Y, and Nb variations in volcanic rocks; *Contrib. Mineral. Petrol.* **69(1)** 33–47.

Pearce J A 1982 Trace element characteristics of lavas from destructive plate boundaries; *Andesites* **4(1)** 528–548.

Pearce J A 1983 Role of the sub-continental lithosphere in magma genesis at active continental margins; *J. Electrochem. Soc.* **147(6)** 2162–2173.

Pearce J A and Peate D W 1995 Tectonic implications of the composition of volcanic ARC magmas; *Annu. Rev. Earth Planet. Sci.* **23(23)** 251–285.

Pearce J A and Stern R J 2006 Origin of Backarc Basin Magmas: Trace element and isotope perspectives; *Am. Geophys. Union* **166** 63–86.

Peccerillo R and Taylor S R 1976 Geochemistry of Eocene calc–alkaline volcanic rocks from the Kastamonu area, northern Turkey; *Contrib. Mineral. Petrol.* **58(1)** 63–81.

Pin C, Majerowicz A and Wojciechowska I 1988 Upper Paleozoic oceanic crust in the Polish Sudetes: Nd–Sr isotope and trace element evidence; *Lithos* **21(3)** 195–209.

Santosh M 2010 Assembling North China Craton within the Columbia supercontinent: The role of double-sided subduction; *Precamb. Res.* **178(1–4)** 149–167.

Sengör A M C, Natal'in B A and Burtman V S 1993 Evolution of the Altaid tectonic collage and Paleozoic crustal growth in Eurasia; *Nature* **364** 299–307.

Shao J A 1989 Continental crust accretion and tectonomagmatic activity at the northern margin of the Sino-Korean plate; *J. Southeast Asian Earth Sci.* **3(1–4)** 57–62.

Song X Y, Zhou M F, Cao Z M and Robinson P T 2004 Late Permian rifting of the South China Craton caused by the Emeishan mantle plume; *J. Geol. Soc.* **161(5)** 773–781.

Stampfli G M and Borel G D 2002 A plate tectonic model for the Paleozoic and Mesozoic constrained by dynamic plate boundaries and restored synthetic oceanic isochrones; *Earth Planet. Sci. Lett.* **196(1–2)** 17–33.

Sun S S and McDonough W F 1989 Chemical and isotopic systematics of oceanic basalts: Implication for mantle composition and processes; *Geol. Soc. London Spec. Publ.* **42** 313–345.

Tang K D and Yan Z Y 1993 Regional metamorphism and tectonic evolution of the Inner Mongolian suture zone; *J. Metamorph. Geol.* **11(4)** 511–522.

Trail D, Watson E B and Tailby N D 2011 The oxidation state of Hadean magmas and implications for early Earth's atmosphere; *Nature* **480** 79–83.

Wang X, Xu Z Y, Liu Z H, Wang W F, Wei L Y, Li F, Liu M N, Chang L, Li G Y and Liu X 2015 Geochronological, geochemical characteristics and geological significance of deyanqimiao amphibolite series in Inner Mongolia; *J. Earth Sci. Environ.* **37(02)** 1–10 (in Chinese with English abstract).

Wang F, Xu W L, Meng E, Cao H H and Gao F H 2012 Early Paleozoic Amalgamation of the Songnen–Zhangguangcai Range and Jiamusi Massifs in the eastern segment of the Central Asian Orogenic Belt: Geochronological and geochemical evidence from granitoids and rhyolites; *J. Asian Earth Sci.* **49(3)** 234–248.

Weaver B L 1991 The origin of ocean island basalt end-member compositions: Trace element and isotopic constraints; *Earth Planet. Sci. Lett.* **104(2–4)** 381–397.

Wilde S A, Zhao G C and Sun M 2002 Development of the North China Craton during the Late Archaean and its amalgamation along a major 18 Ga collision zone including speculations on its position within a global Paleoproterozoic Supercontinent; *Gondwana Res.* **5(1)** 85–94.

Winchester J A and Floyd P A 1977 Geochemical discrimination of different magma series and their differentiation products using immobile elements; *Chem. Geol.* **20(4)** 325–343.

Windley B F, Alexeiev D, Xiao W J, Kroner A and Badarch G 2006 Tectonic models for accretion of the Central Asian Orogenic Belt; *J. Geol. Soc.* **164(12)** 31–47.

Xia L Q, Xia Z C, Xu X Y, Li X M and Ma Z P 2007 The discrimination between continental basalt and island arc basalt based on geochemical method; *Acta Petrol. Mineral.* **26** 77–89 (in Chinese with English abstract).

Xiao W J, Windley B F, Hao J and Zhai M G 2003 Accretion leading to collision and the Permian Solonker suture, Inner Mongolia, China: Termination of the central Asian orogenic belt; *Tectonics* **22(6)** 8–1.

Xiao W J, Windley B F, Badarch G, Sun S, Li J, Qin K and Wang Z 2004 Palaeozoic accretionary and convergent tectonics of the southern Altaids: Implications for the growth of Central Asia; *J. Geol. Soc.* **161(3)** 339–342.

Xiao W J, Windley B F, Huang B C, Han C M, Yuan C, Chen H L, Sun M, Sun S and Li J L 2009 End-Permian to mid-Triassic termination of the accretionary processes of the southern Altaids: Implications for the geodynamic evolution, Phanerozoic continental growth, and metallogeny of Central Asia; *Int. J. Earth Sci.* **98(6)** 1189–1287.

Xu B, Charvet J, Chen Y, Zhao P and Shi G 2013 Middle Paleozoic convergent orogenic belts in western Inner Mongolia (China): Framework, kinematics, geochronology and implications for tectonic evolution of the Central Asian Orogenic Belt; *Gondwana Res.* **23(4)** 1342–1364.

Xu M J, Li C, Xu W, Xie C M, Hu P Y and Wang M 2014 Petrology, geochemistry and geochronology of gabbros from the Zhongcang ophiolitic mélange, central Tibet: Implications for an intra-oceanic subduction zone within the Neo-Tethys Ocean; *J. Earth Sci.* **25(2)** 224–240.

Yang Q Y, Santosh M and Dong G C 2014 Late Palaeoproterozoic post-collisional magmatism in the North China Craton: Geochemistry, zircon U–Pb geochronology, and Hf isotope of the pyroxenite–gabbro–diorite suite from Xinghe, Inner Mongolia; *Int. Geol. Rev.* **56(8)** 959–984.

Yuan H L, Gao S, Dai M N, Zong C L, Günther D, Fontaine G H, Liu X M and Diwu C R 2008 Simultaneous determinations of U–Pb age, Hf isotopes and trace element compositions of zircon by excimer laser-ablation quadrupole and multiple-collector ICPMS; *Chem. Geol.* **247(1–2)** 100–118.

Zhai M G and Santosh M 2011 The early Precambrian odyssey of the North China Craton: A synoptic overview; *Gondwana Res.* **20(1)** 6–25.

Zhai M, Bo H U, Peng P and Zhao T 2014 Meso-Neoproterozoic magmatic events and multi-stage rifting in the NCC; *Earth Sci. Front.* **21** 100–119 (in Chinese with English abstract).

Zhang S H, Zhao Y and Song B 2006 Hornblende thermobarometry of the Carboniferous granitoids from the Inner Mongolia paleo-uplift: Implications for the geotectonic evolution of the northern margin of North China block; *Mineral. Petrol.* **87(1)** 123–141.

Zhang S H, Zhao Y, Ye H, Liu J M and Hu Z C 2014 Origin and evolution of the Bainaimiao arc belt: Implications for crustal growth in the southern Central Asian orogenic belt; *Geol. Soc. Am. Bull* **126(9–10)** 1275–1300.

Zhang W and Jian P 2008 SHRIMP dating of early Paleozoic granites from North Damaoqi, Inner Mongolia; *Acta Geol. Sin.* **82(6)** 779–787 (in Chinese with English abstract).

Zhang W, Jian P, Kröner A and Shi Y R 2013 Magmatic and metamorphic development of an early to mid-Paleozoic continental margin arc in the southernmost Central Asian Orogenic Belt, Inner Mongolia, China; *J. Asian Earth Sci.* **72(4)** 63–74.

Zhang X H, Zhang H F, Jiang N, Zhai M G and Zhang Y B 2010 Early Devonian alkaline intrusive complex from the northern North China craton: A petrological monitor of post-collisional tectonics; *J. Geol. Soc.* **167(4)** 717–730.

Zhao G C, Wilde S A, Cawood P A and Sun M 2001 Archean blocks and their boundaries in the North China Craton: Lithological, geochemical, structural and P–T path constraints and tectonic evolution; *Precamb. Res.* **107(1–2)** 45–73.

Zhao G C, Wilds S A, Guo J H, Cawood P A, Sun M and Li X 2010 Single zircon grains record two Paleoproterozoic collisional events in North China Craton; *Precamb. Res.* **177(3)** 266–276.

Zhao G C and Zhai M G 2013 Lithotectonic elements of Precambrian basement in the North China Craton: Review and tectonic implications; *Gondwana Res.* **23(4)** 1207–1240.

Zhao S, Xu W L, Wang W, Tang J and Zhang Y H 2014 Geochronology and geochemistry of Middle-Late Ordovician granites and gabbros in the Erguna region, NE China: Implications for the tectonic evolution of the Erguna Massif; *J. Earth Sci.* **25** 841–853.

Zhou J L, Shao S, Luo Z H, Shao J B, Wu D T and Rasoamalala V 2015 Geochronology and geochemistry of Cryogenian gabbros from the Ambatondrazaka area, east-central Madagascar: Implications for Madagascar-India correlation and Rodinia paleogeography; *Precamb. Res.* **256(8)** 256–270.

Corresponding editor: R K Srivastava